

https://dspace.org/

Magmatic evolution of the Schiel Alkaline Complex Bushveld large igneous province South Africa

A Hoss; R Klemd; Robert Bolhar; K.M Haase

ELSEVIER SCIENCE BV
https://hdl.handle.net/10539/40924
WOS

Downloaded from a DSpace repository. https://dspace.org/

LITHOS 466-467 (2024) 107464

Contents lists available at ScienceDirect

LITHOS

journal homepage: www.elsevier.com/locate/lithos

Magmatic evolution of the Schiel Alkaline Complex, Bushveld large igneous province, South Africa

Alica Höss [a,*], Reiner Klemd [a], Robert Bolhar [b], Karsten M. Haase [a], Joshua Ramos [a], Elena Geiger [a], Sönke Brandt [a], Torsten Graupner [c]

[a] GeoZentrum Nordbayern, Friedrich-Alexander-Universität Erlangen-Nürnberg, 91054 Erlangen, Germany
[b] School of Geosciences, University of the Witwatersrand, Braamfontein 2001, South Africa
[c] Bundesanstalt für Geowissenschaften und Rohstoffe, D-30655 Hannover, Germany

ARTICLE INFO

Keywords:
Alkaline complex
Bushveld LIP
Crustal assimilation
Fractional crystallization
Nd-Hf isotope compositions
Rare earth elements

ABSTRACT

The Paleoproterozoic Schiel Alkaline Complex (SAC) in the Limpopo Belt is a composite pluton that coevally formed with the layered intrusion of the Bushveld large igneous province. The SAC is mainly composed of alkaline felsic rocks, pyroxenite, gabbro, syenodiorite/−gabbro, and minor carbonatite and gabbroic dikes. Here we present a new geochemical, geochronological, and isotopic study of the felsic and (ultra)mafic rock suites of the western SAC. The whole rock Sm—Nd isotope study of the felsic rocks revealed $\varepsilon Nd_{2059\ Ma}$ values between −6.5 and − 3.8, while those of the syenodiorite/−gabbros and gabbros vary from −7.9 to −8.8, and − 4.3 to +1.1, respectively. The pyroxenites have $\varepsilon Nd_{2059\ Ma}$ values of +7.4 to +2.7. The Lu—Hf isotope study displays $\varepsilon Hf_{2059\ Ma}$ values of −15.9 to −9.0 for the syenites, alkali granites and syenodiorite/−gabbros, and significantly higher $\varepsilon Hf_{2059\ Ma}$ of −3.1 to +3.4 for the gabbros. LA-SF-ICPMS U—Pb zircon dating yields 2079 ± 10 Ma and 2088 ± 30 Ma for the syenodiorite/−gabbros, and 2086 ± 51 Ma and 2107 ± 30 Ma for the gabbros. In conjunction with published data from the eastern SAC, we propose a close petrogenetic link between the mafic and felsic rocks of the SAC. The positive εNd and εHf values of the pyroxenite and gabbro favor a depleted mantle source, while variable εNd and εHf values, and trace element ratios of the gabbros are ascribed to crustal contamination during magma ascent. The felsic rocks, however, mainly formed by fractional crystallization from the gabbros as revealed by major and trace element correlation trends, isotopic data and thermodynamic modelling.

1. Introduction

Large igneous provinces (LIP) are the products of massive partial melting events in the upper mantle that caused voluminous eruptions of lavas as well as intrusions in the crust (Ernst, 2014). The lavas are typically tholeiitic basalts that cover thousands of square kilometers on both continents and on the seafloor, and are believed to have formed in a thermal mantle plume head (e.g., Silver et al., 2006; Ashwal, 2021). These flood basalts are often associated with composite igneous complexes consisting of alkaline and carbonatitic rocks (Ernst and Bell, 2010; Natali et al., 2018; Simonetti et al., 1995). The formation of the alkaline magmatism is poorly understood and, in some cases, the alkaline melts are believed to have formed in mantle plumes (Basu et al., 1993). In other models, the alkaline melts are interpreted to have formed at the margin of mantle plumes possibly from melting subcontinental lithospheric mantle (Beccaluva et al., 2020; Black et al., 2021; Gibson et al., 2006; Natali et al., 2013). The alkaline rocks and the associated carbonatites are usually highly enriched in incompatible elements, including light rare earth elements (LREE), Nb, and Ta and, thus, have been studied for their potential as deposits of critical elements (e.g., Decrée et al., 2020; Mariano, 1989).

The Bushveld Igneous Complex that formed ca. 2.06–2.05 Ga ago (Mungall et al., 2016; Scoates et al., 2021, and references therein), is part of the Bushveld Large Igneous Province, one of the largest LIPs on Earth (e.g., Ernst and Bell, 2010). Similar ages of the Schiel Alkaline Complex (2.06–2.05 Ga, Graupner et al., 2018; Laurent and Zeh, 2015) and the Phalaborwa Carbonatite Complex (ca. 2.06 Ga, Le Bras et al., 2022; Wu et al., 2011), indicate their formation within the Bushveld LIP, however, aspects of its formation are still being debated (e.g., Ernst and Bell, 2010; Hatton, 1995; Zirakparvar et al., 2019). Most authors suggest

* Corresponding author.
E-mail address: alica.hoess@fau.de (A. Höss).

https://doi.org/10.1016/j.lithos.2023.107464
Received 21 July 2023; Received in revised form 2 December 2023; Accepted 8 December 2023
Available online 14 December 2023
0024-4937/© 2023 Elsevier B.V. All rights reserved.

that the formation of the various intrusions of the Bushveld LIP was induced by a mantle plume (Ashwal, 2021; Hatton, 1995; Zirakparvar et al., 2019). The Schiel Alkaline Complex (SAC) and the Phalaborwa Carbonatite Complex (PCC) have been assigned to the early phase of the Bushveld LIP formation, comprising mainly rhyolitic and subordinate mafic lavas of the Rooiberg Group (Verwoerd et al., 1995). The PCC is well-studied due to Cu, phosphate, and vermiculite mining, and its REE potential (Decrée et al., 2020; Verwoerd and Du Toit, 2006; Wilson, 1989; Wu et al., 2011). In contrast, the SAC has received comparably minor attention so far (e.g., Verwoerd and Du Toit, 2006).

Laurent and Zeh (2015) reported unradiogenic zircon $\varepsilon Hf(t_{2060})$ values from −12.9 to −17.1 for syenite and websterite samples of the eastern part of the SAC, and a negative bulk rock $\varepsilon Nd(t_{2060})$ value of −3.6 was presented for syenite by Barton et al. (1996). Samarium-Nd ($\varepsilon Nd(t)$ −8.6 to −6.0) and Rb—Sr ($^{87}Sr/^{86}Sr(t)$ 0.70819–0.70859) isotope data for whole-rock syenite and pyroxenite samples and mineral separates were interpreted to indicate an origin from an isotopically enriched and slightly variable source (Graupner et al., 2018). However, Laurent and Zeh (2015) suggested that the syenites fractionated from mafic magmas that formed by melting of an enriched sub-continental lithospheric mantle (SCLM), which had been metasomatized during an unspecified 2.88–2.75 Ga subduction event. It was argued that differing zircon $^{176}Lu/^{177}Hf$ and εHf_t values of coeval syenite and websterite are related to their formation from SCLM that was variably contaminated by TTG-derived sediments or ancient mafic crust. Lithospheric mantle melting may have been triggered by the arrival of a deep mantle plume (Laurent and Zeh, 2015).

We present a comprehensive, major-, trace-, and isotope-geochemical dataset of the ultramafic, mafic, and felsic intrusive rocks of the poorly-studied western segment of the SAC. In conjunction with previously published data, age constraints are combined with major and trace element trends, trace element ratios, and isotopic data to understand the relation between pyroxenites, gabbros, syenites, and alkali granites of the eastern and western SAC and to identify the magma source. Variations in the isotopic data and thermodynamic modelling are further used to discuss magma evolution processes such as fractional crystallization and crustal assimilation.

2. Geological setting

The Limpopo Belt (LB) of southern Africa is exposed in Zimbabwe, Botswana, and South Africa (Fig. 1), covering an area of ca. 185.000 km^2 over a length of ~600 km and a width of 250 km. The LB is a high-grade metamorphic terrane, bounded by the Zimbabwe Craton in the north and the Kaapvaal Craton in the south. It is commonly subdivided into three major zones, namely the Northern Marginal Zone, the Central Zone, and the Southern Marginal Zone, which are separated by inward-dipping reverse-sense shear zones (Barton et al., 2006; Mason, 1973; van Reenen et al., 2011a). The SAC is situated in the Southern Marginal Zone in South Africa and extends over an area of ~133 km^2. The Southern Marginal Zone forms an ENE-WSW trending unit, which is framed by prominent ductile shear zones that parallel the regional trend. The boundary between the Southern Marginal Zone and the Kaapvaal Craton to the south is marked by the Hout River Shear Zone (Fig. 1), whereas the Palala Shear Zone forms the northern boundary.

The Southern Marginal Zone comprises intensely deformed granulite-facies gneisses that underwent a post-peak high-temperature decompression-cooling metamorphic evolution (Roering et al., 1992;

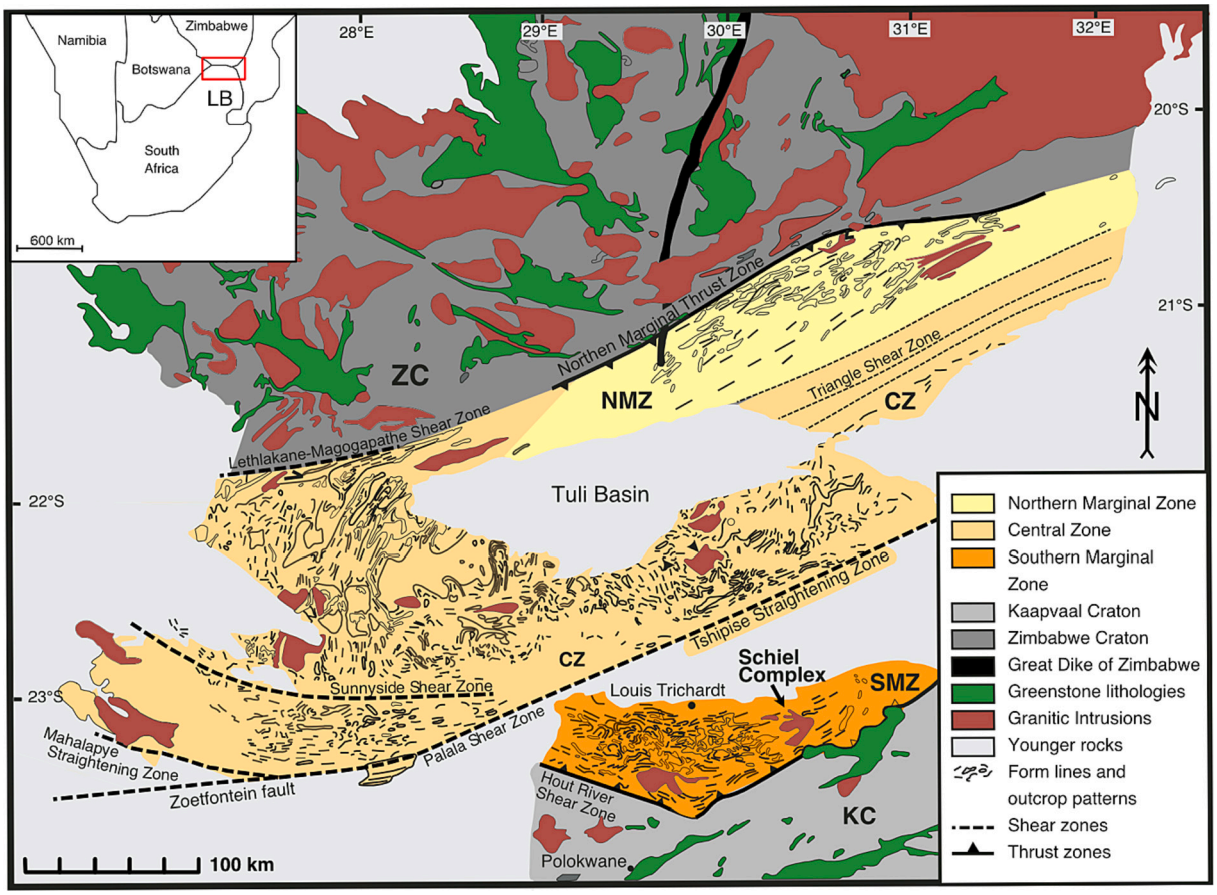


Fig. 1. Geological overview map of the Limpopo Belt (LB) in South Africa and its subdivision into the Northern Marginal Zone (NMZ), Central Zone (CZ), and Southern Marginal Zone (SMZ). Granitic intrusions and greenstone lithologies are included as well as larger tectonic structures. The Schiel Complex is one of several alkaline granitoid intrusions of the SMZ (modified after van Reenen et al., 2011b).

van Reenen et al., 2011b). The Southern Marginal Zone is dominated by large volumes of the enderbitic Baviaanskloof Gneiss with minor intercalations of the 3.15 Ga Bandelierkop Formation (Barton et al., 1996), which consists of metapelitic and mafic to ultramafic gneisses. A long-lasting granulite-facies metamorphic event between 2.72 and 2.68 Ga (e.g., Roering et al., 1992; van Reenen et al., 2011b) was followed by several magmatic intrusions after the main deformation phase, including the late- to post kinematic Matok Pluton at 2.67–2.66 Ga, the 2.64 Ga leucocratic anatectic gneisses, the post-tectonic Palmietfontein granites (2.46 Ga), and the 2.06 Ga SAC (Barton et al., 1996; Laurent and Zeh, 2015; Walraven et al., 1992). In summary, the rocks of the Southern Marginal Zone are interpreted to represent the high-grade metamorphic equivalent of the northern Kaapvaal Craton (van Reenen et al., 2011b).

The SAC intruded the Baviaanskloof Gneiss (Stettler et al., 1993), and is subdivided into a larger, horseshoe-shaped eastern part (ESAC) and a smaller western part (Fig. 2). The NE-SW striking and ~ 4 km wide Kudus River Lineament (Fig. 2) and the WSW-ENE striking N'tabalala Shear Zone occur close to the SAC. The SAC post-dates the formation of the shear zones and is not affected by any tectonic deformation, implying it is a post-collisional intrusion (Graupner et al., 2018; Laurent and Zeh, 2015). Nevertheless, Du Toit (1979) suggested that the melts forming the SAC were emplaced along pre-existing structures as suggested by their similar strike directions.

The exposed eastern SAC comprises apatite-magnetite-vermiculite mineralization within pyroxenite, phoscorite, melasyenite (sensu lato), (quartz)-syenite, alkali granite, and Bandelierkop Gneiss as country rocks. Biotite-hornblende-rich granites, syenites, and quartz-syenites form NW-SE striking hill chains, whereas the southern limb of the quartz-syenite strikes NE-SW parallel to the Kudus River Lineament. Elliptic-shaped syenodiorite/−gabbro and some gabbroic dikes crop out ~20 km to the west (Du Toit, 1979; Graupner et al., 2018). Geophysical investigations of Stettler et al. (1993) revealed a pyroxenite-carbonatite core, and associated glimmerite and phoscorite in the eastern SAC. The western SAC mainly consists of alkali granites, (quartz)-syenites, melasyenites, gabbros, pyroxenites, and NE-SW striking gabbroic dikes. Stettler et al. (1993) suggested that the eastern SAC formed during two magmatic episodes, with the first magmatic episode comprising the formation of an early pyroxenite-carbonatite core that was intruded by syenite and quartz syenite, followed by the emplacement of pyroxene-amphibole granite in the center of the eastern unit. The second magmatic episode is represented by the emplacement of a syenogabbro body (referred to as syenodiorite/−gabbro in this study) ~20 km west of the eastern unit that is crosscut by numerous NE-SW and NW-SE striking gabbroic dikes (Stettler et al., 1993). Walraven et al. (1992) presented Pb-isotopic ages of 2059 ± 35/36 Ma for various lithologies of the complex. U—Pb zircon ages of syenites and an associated fenitized granite indicate timing of the SAC intrusion at ca 2.0 Ga to 1.85 Ga (Barton et al., 1996). More recently, in situ U—Pb zircon dating by Laurent and Zeh (2015) revealed more precise ages of 2051 ± 6 Ma for two syenite samples and 2054 ± 4 Ma for a websterite sample, while Graupner et al. (2018) reported zircon U—Pb ages of 2050.1 ± 9.9 Ma for two syenite samples, and 2060.5 ± 5.0 Ma and 2059.8 ± 4.0 Ma for two phoscorite samples from the eastern SAC.

3. Material and methods

In total, 97 unweathered samples, comprising syenites and granites ($n = 73$), gabbroic dikes ($n = 8$), gabbros ($n = 5$), and pyroxenites ($n = 3$)

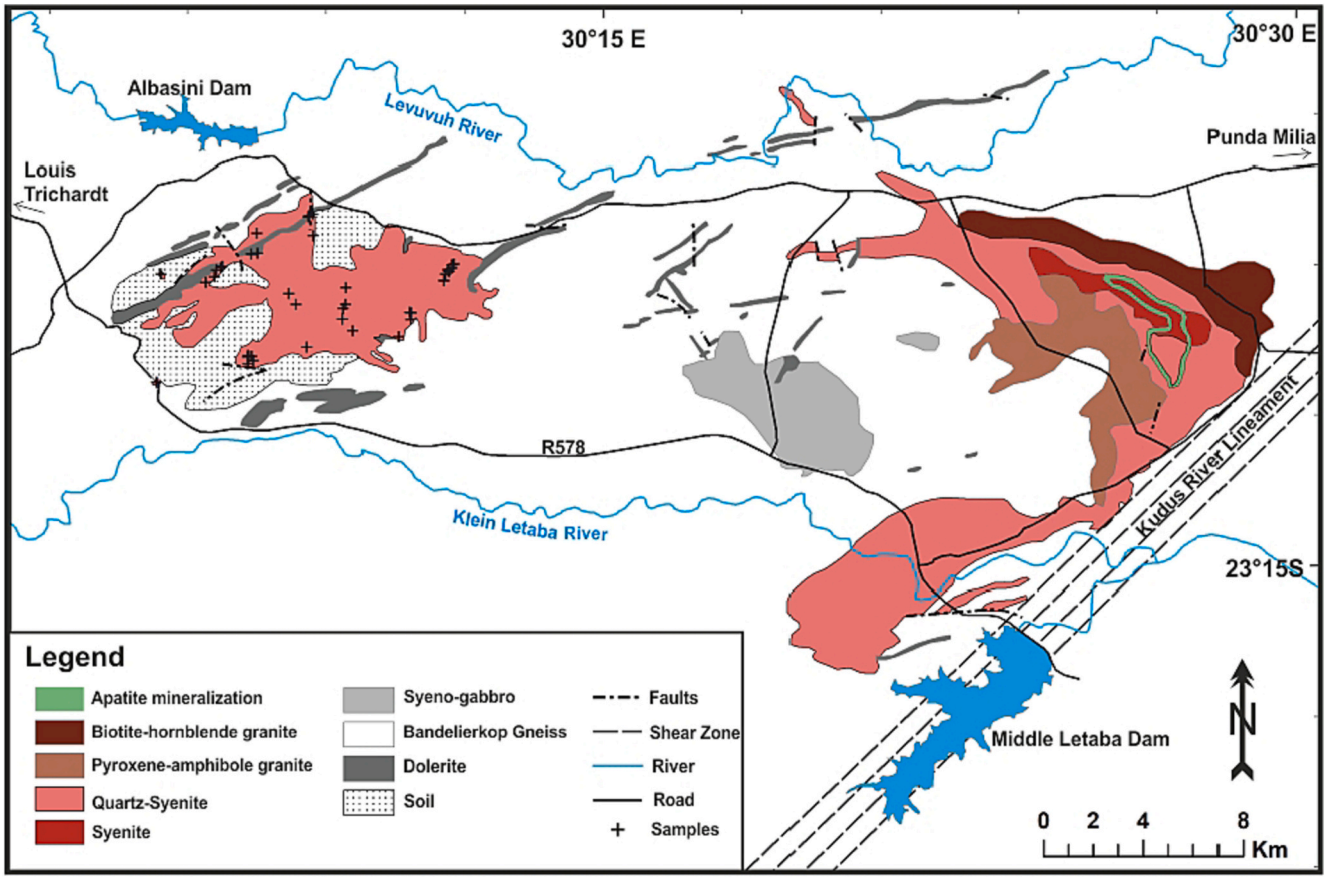


Fig. 2. Geological map of the Schiel Alkaline Complex and its main lithologies, including granites, syenites, syenodiorite/−gabbros, and mafic dikes (modified after Graupner et al., 2018). Small scale variations between syenite and alkali granite, as well as pyroxenite and gabbro are not displayed. The Schiel complex is divided into the larger, horseshoe-shaped eastern part and the smaller western part, which forms the focus in this study.

from the western SAC, and syenodiorite/−gabbros (n = 4) from in-between the eastern and western parts were examined. The bulk rock composition of all samples was determined on a Spectro Xepos HE X-ray fluorescence spectrometer at the GeoZentrum Nordbayern, University Erlangen-Nürnberg. The measurements of major oxides as well as selected trace elements were conducted on fused glass disks. The precision of most elements is <0.5% RSD and accuracy is <6.5%, with the exception of <9.5% for P_2O_5, <8.7% for Ba, <9.4% for Cr, <19.7 for Ga, <23.3% for Th, <9.4 for V, and < 16.1% for Zn, respectively. The results and the averages of international rock standards analyzed with the samples are provided in the supplementary Table A1.

Whole-rock trace elements were conducted on bulk rock powders using an Agilent ICP-AES 5100 (inductively coupled plasma atomic emission spectroscopy) after 4-acid digestion of the beads (method ME-4ACD81) by "ALS" (Ireland). The precision of most elements is better than 5.5%, with the exception of Cs (6.6%), Cd (6.4%), Co (7.5%), Li (20.2%), and W (12.9%). The accuracy is better than 8%, except for Ce (14.2%), Cr (14.3%), Lu (8.8%), Pr (15.6), Ta (28.6), and Li (30%). A list of selected trace elements, including the light and heavy (H)REE, for all lithologies and two representative standard measurements is given in Table 1. Additionally, all sample and standard measurements are included in the supplement Table A1.

The bulk rock Sm—Nd and Lu—Hf isotopic composition of nine syenites and alkali granites, four syenodiorite/−gabbro, five gabbro, and two pyroxenite samples from the western SAC was determined at the GeoZentrum Nordbayern (Table 2). Additional felsic samples from the eastern part of the complex were measured for comparison (suppl. Table A2). Prior to the measurements, the trace element concentrations of Sm, Nd, Lu, and Hf in all samples were determined by solution Thermo X-Series2 quadrupole ICP-MS. The sample solutions were mixed with a Be-In-Rh-Bi internal standard solution before being introduced into the plasma via a Cetac Aridus II desolvating nebulizer. A mixed Li-Ce-In-U solution was used to obtain maximum sensitivity and low oxide production (Ce/CeO > 5000). The BHVO-2 Hawaiian rock standard was used for accuracy and reproducibility over the period of the analysis.

For the isotope measurements, Nd was separated using standard column procedures and Hf was purified using the methods described in Myeong et al. (2023). Both hot plate digestion and bomb digestion were employed. For Nd isotopes both digestion methods yield identical results. With respect to Hf isotopic compositions, both methods yield identical values in the case of two samples (RS-115, SC21–1), but produce slightly different values (difference of approx. 1 epsilon unit) in relation to the analytical uncertainty for samples RS-86 and RS21–2, suggesting partial incomplete digestion possibly due to the presence of zircon. The calculation of the isotopic uncertainties is included in the supplement Table A2.

Neodymium isotope measurements were conducted using a Thermo Fisher Triton thermal ionization multi-collector mass spectrometer in static mode. The measurements were corrected for mass fractionation assuming a $^{146}Nd/^{144}Nd$ ratio of 0.7219. Samarium interference on mass 144 was corrected by the measured ^{147}Sm values. The in-house Nd isotope standard yielded 0.511538 ± 0.000006 (2sd, n = 12), which is equivalent to a value of 0.511848 for the La Jolla Nd isotope standard. The data are reported relative to $^{143}Nd/^{144}Nd = 0.511850$ for La Jolla. A Thermo Fisher Scientific Neptune multicollector ICP-MS mode was used in static mode to measure the Hf isotopes. The interfering isotopes Lu and Yb were corrected on-line, but were negligible. The AMES Grenoble Hf standard yielded a $^{176}Hf/^{177}Hf$ value of 0.282164 during the period of measurements. The sample data is reported relative to a $^{176}Hf/^{177}Hf$ value of 0.282160 for this standard (Chauvel et al., 2011). The initial isotope ratios of Nd were calculated using the age of 2059 Ma and the decay constant of 6.54×10^{-12} (Lugmair and Marti, 1978), and $^{143}Nd/^{144}Nd = 0.51315$ for T_{DM} (Blichert-Toft and Puchtel, 2010). For Hf, the decay constant of 1.867×10^{-11} was used (Söderlund et al., 2004). The εNd and εHf values were calculated relative to the chondrite uniform reservoir (CHUR; Bouvier et al., 2008).

Two syenite, three syenodiorite/−gabbro, and two gabbro samples were selected for in situ U-Th-Pb age dating of titanite, monazite, and zircon. Prior to the measurements, titanites in the syenite were selected based on petrographic observations and LA-ICP-MS trace element data. SEM-ED imaging using a Tescan Integrated Mineral Analyzer (TIMA) was conducted on the syenodiorite/−gabbro and gabbro samples to identify and locate titanite, monazite, and zircon. The U-Th-Pb measurements were carried out in the Earthlab at the University of the Witwatersrand using an Applied Spectra/Australian Scientific Instruments (ASI) Resolution 193 nm ArF excimer laser ablation system coupled to a Thermo Fisher Scientific sector-field ICP-MS (Element XR). Single spot analyses were conducted using a repetition rate of 8–10 Hz, a fluence of 2.5–3.0 Jcm^{-2}, and a beam diameter of 30 μm for zircon, titanite, and 10 μm for monazite. Total signal acquisition time was 30 s with 5 s of pre-and post-ablation to determine gas blank and 20 s of ablation measurements. Laser sampling took place in a SE155 dual-volume ablation cell (Laurin Technic, Canberra, Australia), using a mixed He—Ar atmosphere (He 450 ml/min, Ar 1000 ml/min), and a small volume of N_2 (5 ml/min) to enhance signal stability and sensitivity. The following standards were applied: the GJ1 for calibration of zircon with Plešovice and 91,500 zircon as secondary standard, USGS 44069 for monazite with Thomson Mine, Diamantina, Managotry as secondary standard, MKED for titanite with Ontario and Khan River titanites as secondary standard. The LA-ICPMS system was tuned during line scans using NIST 612 glass for maximum sensitivity for ^{238}U and ^{206}Pb, while maintaining oxide levels (ThO+/Th) < 0.1% and the Th/U ratio > 0.95. Data was collected for ^{202}Hg, $^{204}(Pb + Hg)$, ^{206}Pb, ^{207}Pb, ^{208}Pb, ^{232}Th, and ^{238}U, with sampling times ranging from 0.0005 s ($^{202,204}Hg$) to 0.0045 s (^{207}Pb). Each isotope was measured in pulse counting mode except for ^{238}U and ^{232}Th ("triple", including counting or analogue). Data reduction was performed using the iolite extension to the software Igor Pro (Paton et al., 2011) and the add-in VizualAge (Petrus and Kamber, 2012), while graphic presentation and calculation of Concordia and intercept ages was carried out using the software ISOPLOT-R (Vermeesch, 2018). Uncertainties on individual and mean/regression ages are reported as standard error 2SE. An overview of the age data for each sample is given in Table 3 and for each spot, the U-Th-Pb ages, U/Pb, Pb/Pb, and U/Th ratios, laser spot locations, and cathodoluminescence (CL) and back-scattered electron (BSE) images are provided in the supplement (suppl. Table A3, suppl. Folder B).

4. Results

4.1. Petrography of the western SAC lithologies

The exposed rock types of the western SAC include alkali granites, syenites, gabbros, pyroxenites, and gabbroic dikes (Fig. 3). The various rock types display untectonized and partly transitional intrusive contacts (c.f., Graupner et al., 2018). The syenites and alkali granites mainly consist of alkali feldspar, and strongly variable modal contents of quartz and pyroxene. The grain size varies from fine- to coarse-grained and pegmatitic. The predominant mafic mineral phase is green clinopyroxene with variable modal abundances up to >40 vol%, which mostly occurs homogeneously disseminated in the samples. Minor components are quartz, biotite, and plagioclase, whereas accessories are titanite, apatite, allanite, chevkinite, biotite, zircon, epidote, and magnetite. Furthermore, replacement of clinopyroxene by a blueish, secondary amphibole was observed in most samples. Euhedral zircon is closely associated with altered allanite and titanite. Other hydrothermal textures include Na-rich rims around primary orthoclase, irregular perthite, especially flame perthite, sericite, and REE-rich phases precipitated along mineral fractures. The contact between the syenite, alkali granite and the surrounding country rock is marked by leucogranites and syenites, which were partially affected by hydrothermal alteration, as shown by fine-grained epidote veins and epidote inlets between feldspar crystals. However, pervasive hydrothermal alteration, like the

Table 1
The median, average (av.) and standard deviation (sd) of selected trace element concentrations (ppm) in all lithologies of the western Schiel Complex measured by ICP-MS. The standard "AMIS0304" with the below given average composition was used by ALS as internal standard for the given trace elements except for the REE, which were calibrated to the standard "REE1".

	Alkali granite			Syenite			Syenodiorite/−gabbro			Gabbro			Gabbroic dikes			Pyroxenite			AMIS0304	REE1
	median	av.	sd	median	av.	sd	median	av.	sd	median	av.	sd	median	av.	sd	median	av.	sd	av.	av.
Rb	209.0	205.2	52.3	262.5	262.2	75.3	96.2	85.3	58.2	31.2	72.6	109.7	49.9	54.3	15.7	4.0	3.9	1.7	10.8	1009.0
Ba	2900	2859	1017	3980	4104	1691	345	1049	2059	189	204	55	15	15	2	15	15	2	2565	101
Th	104.3	101.3	68.3	70.2	70.2	57.5	10.4	9.9	1.7	3.1	2.9	1.9	1.5	1.7	0.7	0.1	0.1	0.0	447.0	751.0
U	16.6	20.9	24.3	10.9	12.2	10.4	2.2	2.2	0.3	0.9	0.9	0.6	0.4	0.4	0.2	0.2	0.2	0.1	23.8	133.8
Nb	13.8	14.2	7.9	13.3	16.6	8.8	10.3	9.5	4.8	9.1	7.8	3.0	3.5	4.6	2.7	0.3	0.4	0.3	>2500	>2500
Ta	1.0	1.0	0.5	0.9	1.0	0.5	0.5	0.5	0.2	0.5	0.4	0.2	0.2	0.2	0.2	<0.1	<0.1	<0.1	11.9	222.5
La	64.0	92.3	73.3	125.0	144.5	81.9	138.1	160.0	46.2	18.8	29.5	39.0	6.2	8.5	5.2	0.7	0.8	0.3	3790.0	1685.0
Ce	171.3	176.4	115.6	246.0	256.7	111.7	289.3	323.6	93.5	38.0	63.2	81.5	13.2	18.0	11.6	1.4	1.5	0.8	8845.0	3985.0
Pb	43.0	57.3	55.4	32.0	39.5	32.6	21.3	20.6	3.4	9.0	12.1	9.3	3.5	3.3	1.0	10.0	8.3	2.9		
Pr	11.2	17.0	12.1	30.4	33.0	15.0	35.0	37.2	10.1	5.3	8.1	10.2	1.7	2.4	1.6	0.2	0.2	0.1	>1000	413.5
Nd	44.0	61.8	41.6	120.0	132.1	56.7	2140.9	2154.1	459.4	24.2	36.4	44.2	7.7	10.6	7.3	1.2	1.1	0.6	4245.0	1465.0
Sm	9.8	10.7	6.3	22.4	24.5	10.7	148.0	149.7	38.4	6.2	7.7	7.4	2.1	2.9	2.0	0.5	0.4	0.2	611.5	376.5
Zr	297.0	315.0	235.5	344.0	391.5	307.1	25.4	24.2	6.4	105.0	130.0	54.8	50.5	75.1	59.1	7.0	6.7	2.5	1120.0	>10,000
Hf	6.9	7.8	6.0	9.3	9.9	6.9	134.7	163.3	107.1	3.7	3.7	1.3	1.7	2.2	1.5	0.2	0.3	0.1	27.7	495.5
Eu	2.2	2.5	1.3	4.7	5.3	2.4	3.2	3.8	2.2	1.7	2.0	1.3	0.8	1.0	0.5	0.2	0.2	0.1	154.3	22.6
Gd	6.7	7.8	4.2	16.7	18.2	8.6	6.2	6.2	0.4	6.8	7.3	4.7	2.7	3.6	2.3	0.6	0.6	0.2	355.5	433.5
Tb	0.8	0.9	0.5	1.8	2.0	1.0	16.8	15.7	4.2	1.0	1.0	0.4	0.4	0.5	0.3	0.1	0.1	0.0	33.0	98.9
Dy	4.1	4.7	2.5	8.4	9.8	5.0	1.6	1.5	0.4	6.2	6.0	1.9	2.8	3.7	2.3	0.8	0.8	0.2	137.3	871.0
Ho	0.6	0.7	0.4	1.2	1.4	0.8	7.4	7.1	2.3	1.1	1.0	0.3	0.6	0.7	0.4	0.2	0.2	0.0	17.2	193.8
Y	22.2	22.5	13.6	34.3	42.4	27.1	32.0	30.6	9.2	29.7	28.2	8.2	14.7	19.3	11.9	4.6	4.7	1.0	413.0	5590.0
Er	1.8	2.0	1.1	3.0	3.6	2.3	1.2	1.1	0.4	2.5	3.1	1.0	1.7	2.2	1.3	0.5	0.6	0.1	34.7	710.5
Tm	0.2	0.2	0.1	0.4	0.4	0.3	2.7	2.6	0.8	0.3	0.4	0.2	0.2	0.3	0.2	0.1	0.1	0.0	3.3	105.0
Yb	1.5	1.6	0.9	2.3	2.7	1.9	0.3	0.3	0.1	2.1	2.7	1.1	1.6	2.1	1.2	0.5	0.5	0.1	16.7	680.0
Lu	0.2	0.2	0.1	0.3	0.4	0.3	1.9	1.9	0.7	0.3	0.4	0.2	0.2	0.3	0.2	0.1	0.1	0.0	2.0	89.8
∑REY	314.5	401.2	258.3	632.8	677.2	303.0	144.1	196.9	201.4	56.5	76.2	48.3	11.8	11.7	3.7	21.8	20.1	6.6		

Table 2
Sm—Nd and Lu—Hf isotopic compositions of syenites, syenodiorite/−gabbros, gabbros and pyroxenites mainly of the western SAC.

Sample ID	Lithology	$^{143}Nd/^{144}Nd$	2SD	$^{147}Sm/^{144}Nd$	2SD	Initial $^{143}Nd/^{144}Nd$	$^{176}Hf/^{177}Hf$	2SD	$^{176}Lu/^{177}Hf$	Initial $^{176}Hf/^{177}Hf$	εNd (CHUR)[a]	εHf (CHUR)[a]	T(DM) (Ga)[b]
WSD2	Gabbro	0.51204	0.000005	0.14851	0.003	0.510029	0.282273	0.000002	0.0186	0.281544	1.16	2.71	2.58
WSD10	Alkali granite	0.51122	0.000005	0.116447	0.002	0.509638	0.281312	0.000002	0.0036	0.281172	−6.49	−10.54	3.01
WSD18	Syenite	0.51130	0.000005	0.118503	0.002	0.509697	0.281329	0.000002	0.0032	0.281203	−5.33	−9.41	2.94
WSD20	Syenite	0.51133	0.000005	0.118513	0.002	0.509718	0.281300	0.000002	0.0026	0.281197	−4.92	−9.62	2.90
WSD24	Syenite	0.51118	0.000005	0.111954	0.002	0.509664	0.281356	0.000002	0.0036	0.281216	−5.98	−8.97	2.93
WS17	Pyroxenite	0.51371	0.000009	0.247789	0.005	0.510346			0.0950		7.38		2.47
WS25D	Gabbro	0.51193	0.000005	0.150106	0.003	0.50989	0.282722	0.000002	0.0295	0.281564	−1.56	3.40	2.92
WS26	Syenite			0.145552	0.003		0.281275	0.000002	0.0024	0.281180		−10.25	
WS27	Syenite	0.51113	0.000005	0.106558	0.002	0.509689	0.281603	0.000002	0.0107	0.281182	−5.49	−10.18	2.85
WS34	Syenite	0.51127	0.000005	0.117363	0.002	0.509681	0.281438	0.000002	0.0072	0.281157	−5.66	−11.05	2.95
WS36	Gabbro	0.51172	0.000005	0.144582	0.003	0.509763	0.282270	0.000002	0.0227	0.281381	−4.05	−3.10	3.12
WS40	Gabbro	0.51166	0.000005	0.140635	0.003	0.50975	0.282174	0.000002	0.0184	0.281454	−4.29	−0.51	3.09
WS50	Gabbro	0.51177	0.000005	0.145888	0.003	0.509796	0.282236	0.000002	0.0207	0.281424	−3.40	−1.57	3.07
WS59	Syenite	0.51108	0.000005	0.103772	0.002	0.509668	0.281511	0.000002	0.0188	0.280775	−5.91	−24.61	2.86
WS64	Pyroxenite	0.51269	0.000006	0.190078	0.004	0.510109			0.1065		2.74		2.97
WS71	Syenite	0.51119	0.000005	0.104269	0.002	0.509775	0.281530	0.000002	0.0184	0.280809	−3.80	−23.43	2.72
RS86	Syenite[c]	0.511266	0.000004	0.130642	0.003	0.509495	0.281737	0.000002	0.0117	0.281280	−9.3	−6.68	3.43
RS115	Syenite[c]	0.511104	0.000004	0.111322	0.002	0.509595	0.281469	0.000002	0.0083	0.281142	−7.3	−11.59	3.03
SC21–1	Syenodiorite/−gabbro	0.510800	0.000004	0.094394	0.001	0.509520	0.28139	0.000002	0.0058	0.281159	−8.81	−10.98	2.98
SC21–2	Syenodiorite/−gabbro	0.510885	0.000004	0.099752	0.001	0.509533	0.28219	0.000002	0.0254	0.281194	−8.56	−9.73	3.01
SC21–3	Syenodiorite/−gabbro	0.510808	0.000004	0.091733	0.002	0.509564					−7.94		2.91
SC21–4	Syenodiorite/−gabbro	0.511019	0.000004	0.107789	0.002	0.509558	0.28204	0.000002	0.0260	0.281021	−8.07	−15.91	3.05

A decay constant of 6.54×10^{-12} was used for Nd isotopes (Lugmair and Marti, 1978) and 1.867×10^{-11} for Hf isotopes (Söderlund et al., 2004)

[a] εNd(CHUR) and εHf(CHUR) based on the age of 2.059 Ga with CHUR = chondrite uniform reservoir (Bouvier et al., 2008).

[b] Nd T(DM) gives the model ages based on a Depleted Mantle compositions of $^{147}Sm/^{144}Nd = 0.2137$ and $^{143}Nd/^{144}Nd = 0.51315$ (Blichert-Toft and Puchtel, 2010)

[c] Data from the eastern SAC for comparison (this study)

Table 3
U-Th-Pb ages of different minerals in syenite, syenodiorite/−gabbro, and gabbro obtained by LA-SF-ICPMS.

Sample ID	Lithology	Dated minerals	Th/U	Age[a] (Ma)	2SE (Ma)	MSWD	N[b]	Type[a]	Initial $^{207}Pb/^{206}Pb$[c]
WSD18	Syenite	titanite	N.A.	1978	51	2.7	16	$^{207}Pb/^{206}Pb$	0.925
WS27	Syenite	titanite	N.A.	2007	24	3.8	14	$^{207}Pb/^{206}Pb$	0.937
SC-21-02	Syenodiorite/−gabbro	zircon	0.71	2088	30		1	Conc.	
SC-21-03	Syenodiorite/−gabbro	zircon	0.69–1.21	2079	10	6	7	Conc.	
SC-21-03	Syenodiorite/−gabbro	monazite	N.A.	2085	10	22	7	Conc.	
SC-21-01a	Syenodiorite/−gabbro	titanite	N.A.	2079	19	1.4	14	$^{207}Pb/^{206}Pb$	0.987
SC-21-01b	Syenodiorite/−gabbro	titanite	N.A.	1944	28	38	11	$^{207}Pb/^{206}Pb$	0.913
SC-21-01b	Syenodiorite/−gabbro	titanite	N.A.	2112	24	24	7	$^{207}Pb/^{206}Pb$	0.987[d]
WS 50	Gabbro	zircon	0.42	2107	30		1	Conc.	
WS 50	Gabbro	titanite	N.A.	2098	21	9.1	11	$^{207}Pb/^{206}Pb$	1.021
WSD 2	Gabbro	titanite	0.94–5.70	1662	53	1.2	7	$^{207}Pb/^{206}Pb$	0.87
WSD 2	Gabbro	titanite	0.94–5.70	2086	51	0.5	7	$^{207}Pb/^{206}Pb$	0.987[d]

N.A. = not available.
[a] Concordant U—Pb age (Conc.) or discordia intercept age ($^{207}Pb/^{206}Pb$).
[b] Number of individual U—Pb spots used in the age calculation.
[c] Initial $^{207}Pb/^{206}Pb$ calculated for the discordia ages.
[d] Corrected initial $^{207}Pb/^{206}Pb$.

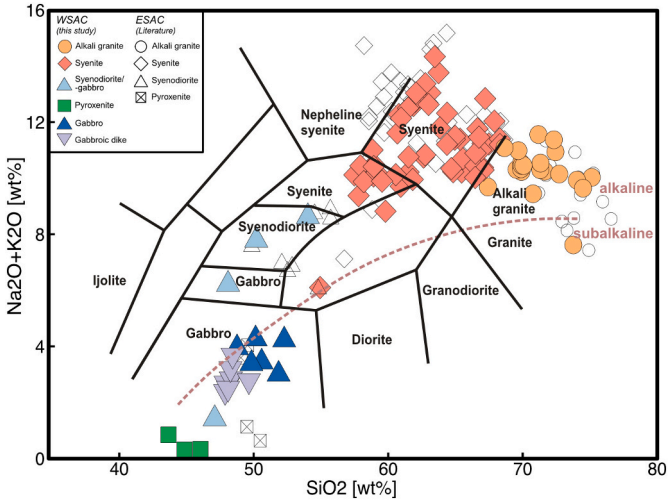


Fig. 3. Total alkali vs silica diagram after Cox et al. (1979) and modified after Wilson (1989a) for plutonic rocks with major elements in wt%. The alkaline and subalkaline boundary (red dotted line) is defined after Miyashiro (1978). The felsic samples mainly plot as alkaline syenites and alkali granites. The mafic rocks plot as gabbros and syenodiorites/−gabbros, while the pyroxenites plot in none of the defined classification fields. The syenites, alkali granites and pyroxenites of the eastern Schiel Complex (hollow symbols) display similar compositions as the western lithologies (Graupner et al., 2018). (For interpretation of the references to colour in this figure legend, the reader is referred to the web version of this article.)

fenitization observed in the eastern SAC, is absent in the western segment.

The interlayered and intrusive gabbros of the western SAC, and those in-between both the eastern and western parts (syenodiorites/−gabbros) are variable in grain size (20–400 μm), usually fine-grained and mainly consist of K-feldspar, plagioclase, clinopyroxene, and amphibole. Anhedral sericitized K-feldspar and plagioclase have sutured grain boundaries or triple points. Amphibole reaches modal abundances up to 40 vol% and is the main mafic mineral in the samples, followed by colorless clinopyroxene. Accessories are biotite, epidote, olivine, and opaque minerals.

The pyroxenites are green to dark grey, fine-to medium-grained, and display a mesh texture due to the presence of secondary serpentine. The major minerals are clinopyroxene, orthopyroxene, and amphibole ± serpentine. Clinopyroxene and orthopyroxene occur with very variable grain sizes from 500 to 3500 μm and range from colorless to brownish colour. Relicts of clinopyroxene occur as inclusions within orthopyroxene and amphibole, while relicts of olivine are present within the serpentine mesh texture or between pyroxenes. Further components are euhedral amphibole, brucite forming coronas around pyroxene grains, and within mineral fractures, serpentine, spinel, and opaque phases. Serpentine only occurs in the western SAC pyroxenites, but is absent in the ultramafic rocks of the eastern SAC.

4.2. *Whole-rock composition of ultramafic to felsic rocks of the eastern and western SAC*

The felsic rocks are mainly alkaline syenites and alkali granites sensu stricto (Fig. 3; Wilson, 1989). The subdivision into syenites and melasyenites (Graupner et al., 2018) was simplified according to Fig. 3, but a subclassification of the samples is given in the electronical supplement (Fig. A1). The mafic lithologies show syenodioritic to gabbroic compositions and were grouped into alkaline syenodiorite/−gabbros, subalkaline gabbros and subalkaline gabbroic dikes based on their geographical location, petrographic characteristic, and isotopic- and geochemical composition. According to the IUGS classification for ultramafic rocks, the pyroxenite samples are hornblende-websterites to hornblende-olivine-websterites. The classification of literature data from the eastern Schiel was adjusted to the subdivision of the western Schiel samples from this study (Fig. 3). The contents of MgO, CaO, $Fe_2O_3^T$ (total iron), P_2O_5, and TiO_2 (Fig. 4) show linear decreasing trends with increasing SiO_2 for the syenites with >60 wt% SiO_2. The concentrations of Na_2O reveal a positive linear, but moderately scattered trend of increasing values with increasing SiO_2 for the syenites and alkali granites. The mafic rocks and the pyroxenites with the lowest SiO_2 content plot somewhat off the trend. The Al_2O_3 and K_2O contents of the syenites have a non-linear trend of increasing values up to ~64 wt% SiO_2 and decreasing values for >64 wt% SiO_2. The mafic rocks contain similar Al_2O_3 concentrations as the least evolved syenites, but lower K_2O, while the ultramafic rocks contain the lowest concentrations of the latter. The content of Cr is highest in the pyroxenites and decreases with increasing SiO_2, whereby the gabbros, the syenodiorite/−gabbros and the less evolved syenites overlap (Fig. 4f). The incompatible element ratios Ba/La and Nb/Zr are similar in the syenites, alkali granites, syenodiorite/−gabbros, and gabbros and overlap at different MgO contents (Fig. 5c, d). Additionally, the syenites and alkali granites show higher and variable chondrite-normalized $(Dy/Yb)_N$ ratios than the gabbros (Fig. 5a).

The median Primitive Mantle (PRIMA)-normalized trace element patterns (Sun and McDonough, 1989) and representative analyses of western SAC rocks, as well as patterns for the rocks from the eastern

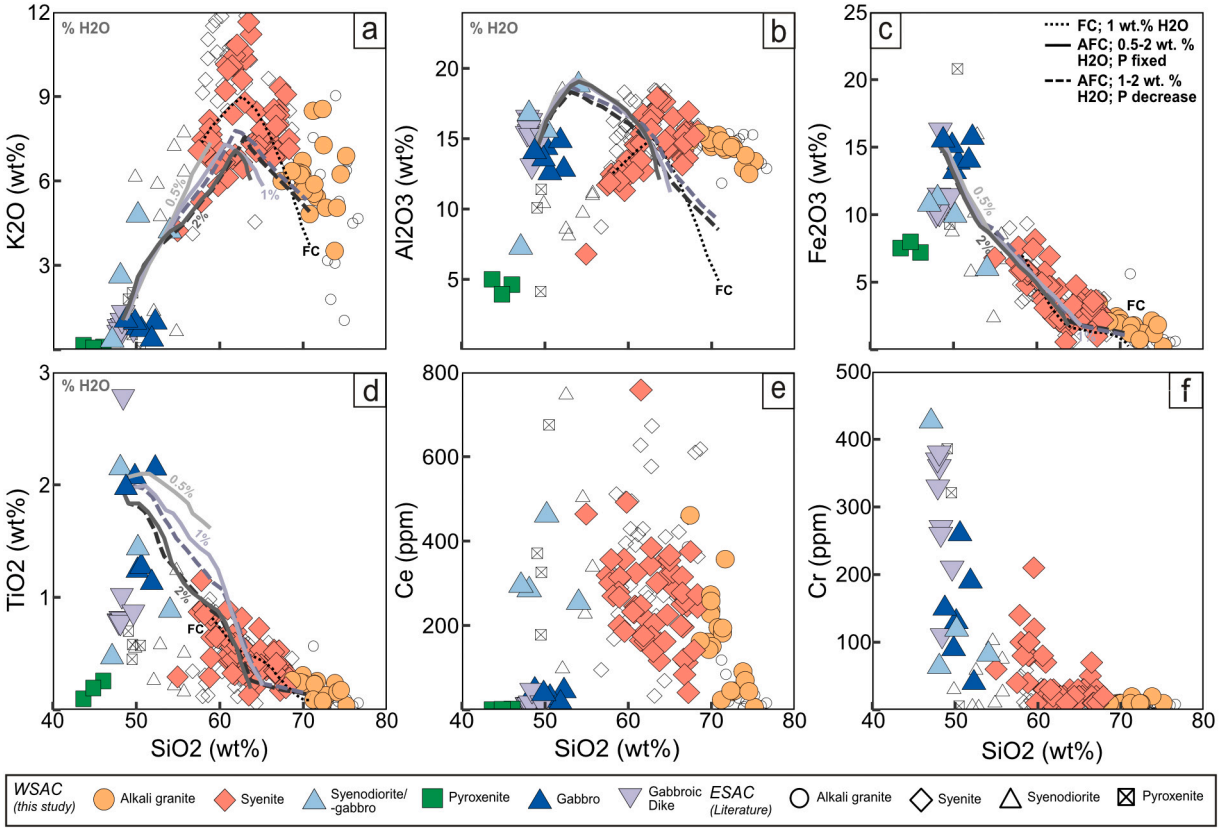


Fig. 4. Harker diagrams with major and trace elements against SiO_2 displaying distinct compositional trends, especially for the syenites and alkali granites. Main oxides in wt% and trace elements in ppm. Fractional crystallization (FC) modelling of major elements was conducted using MELTS for the syenites and alkali granites at 3 kbar and 1 wt% water content. Assimilation-fractional crystallization (AFC) was modelled for the gabbros (0.5, 1, and 2 wt% H_2O) using the composition of Kaapvaal Craton-related metapelite at fixed pressures of 6 kbar and decreasing pressures fom 7 to 2 kbar. Literature data for the eastern SAC shown as hollow symbols (Graupner et al., 2018).

SAC, are shown in Fig. 6. The syenites and alkali granites show a comparable enrichment of highly incompatible trace elements decreasing towards the less incompatible elements (Table 1). Especially Rb, Ba, Th, and U are strongly enriched, while Nb, Ta, and Ti show distinct negative anomalies (Fig. 6a). In comparison, the gabbros show an overall flat trace element pattern with lower concentrations in incompatible elements, except for distinct positive Pb, and negative Nb and Ta anomalies (Fig. 6c). The pyroxenites have similar trace element concentrations to PRIMA, except for positive U and Pb, and negative Th, Nb, and Ta anomalies.

The rare earth elements were normalized to chondrite (McDonough and Sun, 1995) and most samples show patterns of decreasing abundances of LREE towards HREE. The syenites and alkali granites are relatively enriched in LREE and decrease towards the HREE (Fig. 6b). Cerium contents are variable showing positive and negative anomalies ($Ce/Ce^* = 0.5–6.1$), while Eu usually displays a minor negative anomaly ($Eu/Eu^* = 0.7–1.2$). The syenodiorite/−gabbros and the eastern SAC pyroxenites contain similar REE concentrations when compared to the felsic rocks, with a steep decrease from LREE to HREE. The gabbros display minor REE enrichment compared to chondrite with similar concentrations of LREE and HREE, while the pyroxenites have relatively low REE contents.

4.3. Whole-rock isotopic composition

Whole-rock isotopic data of two pyroxenites, five gabbros, eight syenites, and one alkali granites from the western SAC, four syenodiorite/−gabbros, and two syenites from the eastern SAC (RS86, RS 115) are summarized in Table 2. The εNd values for the western SAC rocks were calculated using a crystallization age of 2.059 Ga for the intrusion (Walraven et al., 1992). These values range considerably between the different rock types, but are relatively uniform for the individual rock types. The εNd are lowest in the syenodiorite/−gabbros (−8.8 to −7.9), followed by those of the syenites and alkali granites (−6.5 to −3.8) (Fig. 7a, b). The gabbros have values of −4.3 to +1.1 and the highest εNd are shown by the pyroxenites (εNd = +2.7 to +7.4). The calculated Nd model ages T_{DM} are 3.0–2.7 Ga for the felsic rocks, 3.1–2.9 Ga for the syenodiorite/−gabbros, 3.1–2.6 Ga for the gabbros, and 3.0–2.5 Ga for the pyroxenites (Table 2). The syenites, alkali granites and gabbros display a good correlation of Nd isotope ratios with $^{147}Sm/^{144}Nd$ ratios (Fig. 7a) with a regression of $R^2 = 0.95$. The respective apparent isochron ages (Vermeesch, 2018) yielded 2526.1 ± 53.1 Ma (1SE; MSWD = 7.3) for the syenites, alkali granites, and gabbros (Fig. 7a), and 2211 ± 105 Ma (1SE; MSWD = 3.1) for the syenites and alkali granites alone (not shown). The εHf values for the western SAC also vary strongly between the lithologies (Fig. 7c), and are low for the syenodiorite/−gabbros (− 15.9 to −9.7), syenites and alkali granites (−24.6 to −9.0), and significantly higher for the gabbros (−3.1 to +3.4).

Our Nd and Hf data of the syenites and alkali granites from the western SAC overlap with our data from the eastern SAC (Table 2, suppl. Table A2) and literature whole-rock data of the ESAC (εNd = −8.6 to −6.0; Graupner et al., 2018). Furthermore, previous εHf studies on the ESAC yielded an average of −12.8 for zircon in the felsic rocks (Graupner et al., 2018; Laurent and Zeh, 2015). However, the distinct range of negative to positive εHf and εNd values was not observed in the eastern SAC, where the ultramafic samples also show negative εHf and εNd values (ESAC pyroxenites εNd = −8 to −6; εHf = −17; Graupner et al., 2018; Laurent and Zeh, 2015). Positive εNd values are also absent

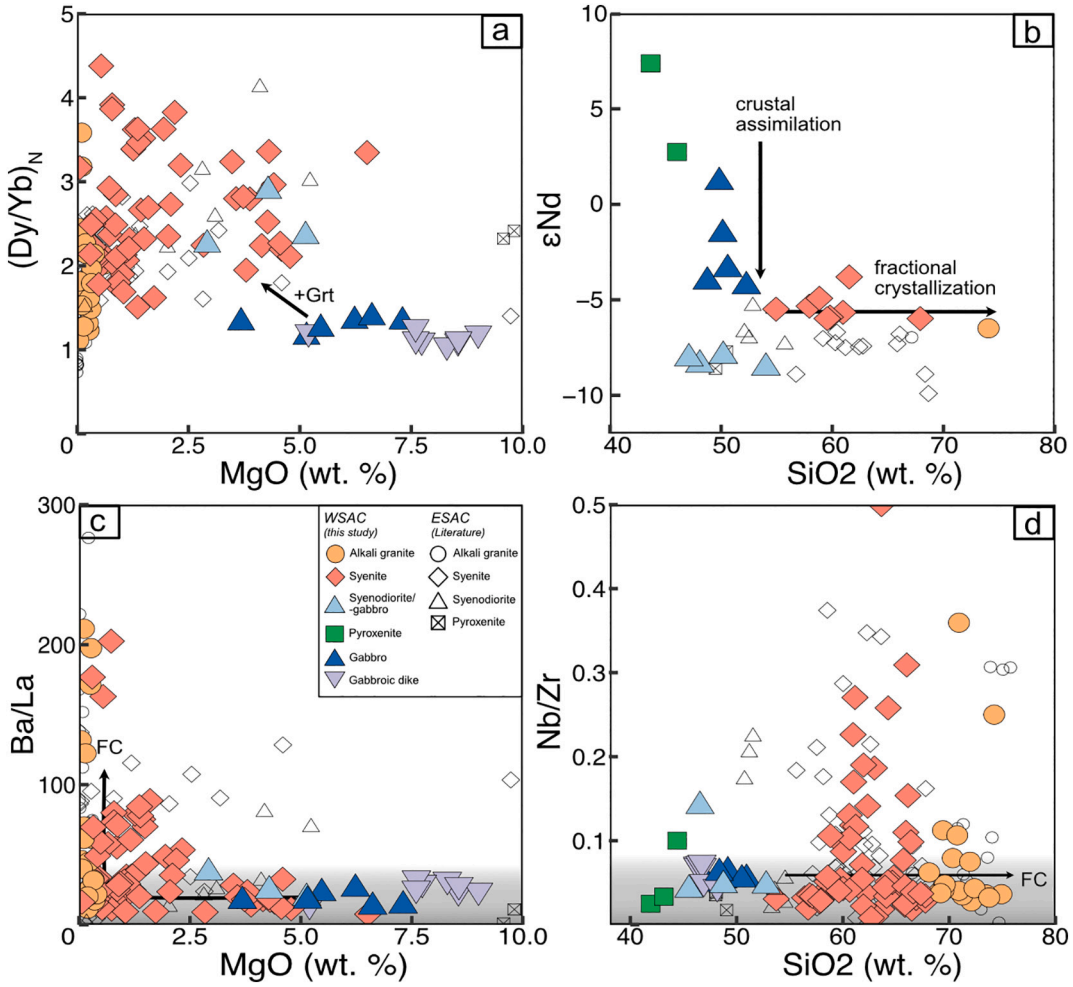


Fig. 5. The isotopic data and trace element ratios of the mafic and felsic rocks of the SAC. (a) Epsilon Nd against MgO (wt%) displaying a changing isotopic composition within the samples. (b, c) Nb/Zr and Ba/La against MgO showing overlapping and continuous trends for the mafic and felsic rocks. (d) Chondrite-normalized Dy/Yb against MgO showing an increase from gabbros to syenites and alkali granites. Literature data for the eastern SAC shown as hollow symbols (Graupner et al., 2018). Grt = garnet, FC = fractional crystallization.

in the apatite data of pyroxenites, phoscorites, and carbonatites from the coeval PCC (Fig. 7c; εNd(t): −7.4 to −3.4; Wu et al., 2011).

4.4. *In situ U—Pb geochronology*

Titanite grains in two syenitic samples (WSD18, WS27), and zircon, monazite, and titanite grains in the three syenodiorite/−gabbro samples (SC-21-01, SC-21-02, SC-21-03) and two gabbro samples (WS50, WSD2) were selected for in situ U—Pb age determinations. All uncertainties are given as double standard error (2SE). The selected titanites include large to small (~200 μm) euhedral wedge-shaped and anhedral grains, without zoning or internal texture (Fig. 8a, b, e, f). Matrix monazites have square to ellipsoid or irregular shapes, straight to sutured grain boundaries and are 200 μm to 1000 μm in diameter. The BSE-images of all grains reveal a homogeneous texture (Fig. 8d). Most zircon grains (100–250 μm in diameter) are euhedral to subhedral or anhedral, and show weak concentric or homogeneous zoning as revealed by the CL-images (Fig. 8c).

In the Tera-Wasserburg diagrams, titanite in the syenite samples WSD18 and WS27 yield discordia lower intercept ages of 1978 ± 51 Ma (MSWD = 2.7) and 2007 ± 24 Ma (MSWD = 3.8), respectively (Fig. 8a, b; Table 3). One analysis in sample WS27 and 8 analyses in sample WSD18 are highly discordant and scatter in the Tera-Wasserburg diagrams, and were, thus, excluded from the age calculations.

Monazite of the syenodiorite/−gabbro SC-21-03 yields a concordia age of 2085 ± 10 Ma (MSWD = 22) (Fig. 8d; Table 3), and titanite discordia intercept ages of 2079 ± 19 Ma (MSWD = 1.4) and 1944 ± 28 (MSWD = 38) for the syenodiorite/−gabbro SC-21-01 (Fig. 8e; Table 3). Titanite in the gabbro samples WS50 and WSD2 yields discordia lower intercept ages of 2098 ± 21 Ma (MSWD = 9.1) (Fig. 8f) and 1662 ± 53 Ma (MSWD = 1.2), respectively (Table 3). Highly discordant spot analyses of monazite and titanite, probably representing Pb loss, were excluded. Additionally, for the two samples SC-21-01b and WSD2 with unreasonably lower $^{207}Pb/^{206}Pb$ (0.913; 0.87), the $^{207}Pb/^{206}Pb$ was corrected to 0.987 based on sample SC-21-01a, which resulted in titanite discordia intercept ages of 2112 ± 24 Ma (MSWD = 24) for the syenodiorite/−gabbro SC-21-01b and 2086 ± 51 Ma (MSWD = 0.5) for the gabbro WSD2 (Table 3).

Concordant zircon ages of 2088 ± 30 Ma (single analysis) and 2079 ± 10 Ma (MSWD = 6) were obtained for the syenodiorite/−gabbro samples SC-21-02 and SC-21-03 (Fig. 8c, Table 3), respectively, and a single near concordant analysis revealed 2107 ± 30 Ma for the gabbro sample WS50 (Table 3). Three strongly discordant spots from each syenodiorite/−gabbro sample (SC-21-02 and SC-21-03) were not further considered. Furthermore, all zircon spot analyses used for age calculation yielded Th/U ratios of 0.42–1.21 (Table 3), which -in combination with the textural characteristics- are typical for magmatic zircon (Corfu, 2003). Supplement Table A3 contains further analytical details and results of the U—Pb measurements of the analyzed minerals and standards used in the present study.

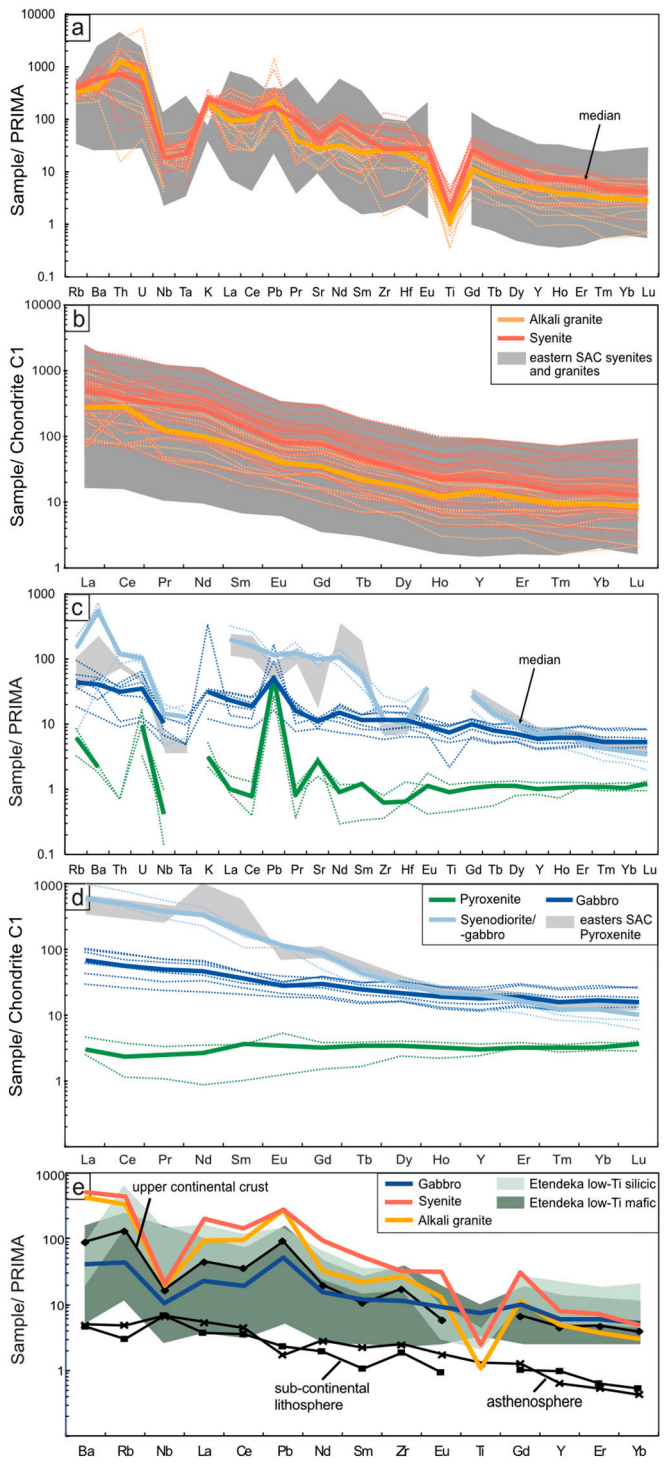


Fig. 6. Multi-element diagrams with representative (dotted) and median trace element compositions of felsic rocks, gabbro, syenodiorite/−gabbro, and pyroxenite of the western SAC (a, c) normalized to Primitive Mantle (Sun and McDonough, 1989), and (b, d) REEs normalized to chondrite C1 (McDonough and Sun, 1995). Literature data of the eastern SAC Graupner et al. (2018) shown as grey fields. (e) Median trace element composition of the syenites and alkali granites and the gabbros compared to literature data from Etendeka silicic and mafic lavas, and associated dikes (Zhou et al., 2020), upper continental crust (Rudnick and Gao, 2014), continental lithospheric mantle (average spinel peridotite; McDonough, 1990), and asthenosphere (OIB x 0.1; Sun and McDonough, 1989; Arndt and Christensen, 1992).

5. Discussion

5.1. Age constraints of the SAC and its relation to the Bushveld large igneous province

The disparity between U/Pb lower intercept ages of titanite between 2098 and 1662 Ma for the syenodiorite/−gabbros and gabbros, coupled with high uncertainties of up to 52 Ma, indicate a prolonged Pb exchange and isotopic resetting, probably due to the low Pb closure temperatures of 550–700 °C in titanite (Cherniak, 1993). Relatively slow cooling or late alteration may, thus, have been the cause for age resetting, as shown by sample WSD2 with an unreasonable low discordia age of 1662 ± 52 Ma (uncorrected) and by the discordia age of 1944 ± 28 Ma (uncorrected) for the syenodiorite/−gabbro SC-01-1b. Younger U—Pb ages of 1850 Ma were also noted by Barton et al. (1996) for the Schiel Complex indicating a possible link to post-crystallization events, such as the Vredefort impact (2023 Ma; Kamo et al., 1996) or to rifting accompanying the deposition in the Soutpansberg trough (Barton et al., 1996). However, the absence of post-crystallization tectonic deformation and the range from 1944 to 1662 Ma does not allow a clear allocation of the resetting event. The corrected age of WSD2 (2086 ± 51 Ma) is within the range of the syenodiorite/−gabbro and gabbro ages of 2079 to 2098 Ma, whereas the corrected age of SC-21-01b (2112 ± 24 Ma) is similar to one gabbro age (WS50; 2107 Ma), representing more reasonable crystallization ages.

In contrast to titanite, zircon and monazite are considered as robust geochronometers due to their high U—Pb closure temperatures (>900 °C) (Cherniak et al., 2004), although monazite is also sensitive to dissolution-precipitation processes, which can modify the isotopic system (Taylor et al., 2016). Monazite and zircon of the syenodiorite/−gabbros and gabbros, however, revealed identical -within error- (near) concordant U—Pb ages (2107–2079 Ma; Table 3) indicating no significant modification of the Pb system and therefore no influence of post-crystallization events.

The syenites and alkali granites U/Pb titanite ages of 2007 ± 24 Ma and 1978 ± 51 Ma are somewhat younger than the zircon ages of the eastern SAC syenites (2050.1 ± 9.9 Ma; 2051 ± 6 Ma) (Graupner et al., 2018; Laurent and Zeh, 2015), which is thought to be due to isotopic resetting that affected the U—Pb isotope system of individual titanite grains. However, the syenodiorite/−gabbro and gabbro U/Pb zircon ages of 2107 ± 30 Ma, 2088 ± 30 Ma, and 2079 ± 10 Ma are similar to those of the phoscorite (2060 ± 4 Ma) and websterite (2054 ± 4 Ma) from the eastern SAC (Graupner et al., 2018; Laurent and Zeh, 2015). The field relationship and the slightly older ages of the syenodiorite/−gabbros and gabbros (Table 3) compared to the syenites and alkali granites indicate a cogenetic relationship between the mafic and felsic lithologies of the SAC, whereby the mafic rocks may represent the early phase of the intrusion. Unfortunately, age dating of the western SAC pyroxenites was not possible due to a lack of suitable material, but it is likely that they represent cumulates cogenetic to the gabbros and felsic rocks. We therefore suggest that the pyroxenites, gabbros, and felsic rocks of the western and eastern SAC formed simultaneously.

Notably, the apparent isochron ages (2526 ± 53.1 Ma) calculated from the Sm—Nd isotopes for the syenites and gabbros are older than the respective U–Pb-derived ages. Hydrothermal alteration, mixing processes, and fractionation of high-pressure phases prior to melt extraction can significantly influence the isotopic system resulting in a discrepancy between whole rock isochron and mineral ages (Bolhar et al., 2023; Chauvel et al., 1985). However, the Sm—Nd and Lu—Hf isotopes correlation and the shift of the apparent isochron towards older ages suggest that hydrothermal alteration and mineral fractionation did not disturb the isotopic system of the syenites and gabbros. Rather, mixing of existing evolved crustal material with the SAC magmas, may have caused the older apparent isochron ages (Chauvel et al., 1985). The pyroxenites were excluded from the calculated isochron as one pyroxenite sample shows higher εNd (+7.4) than the depleted mantle at 2059

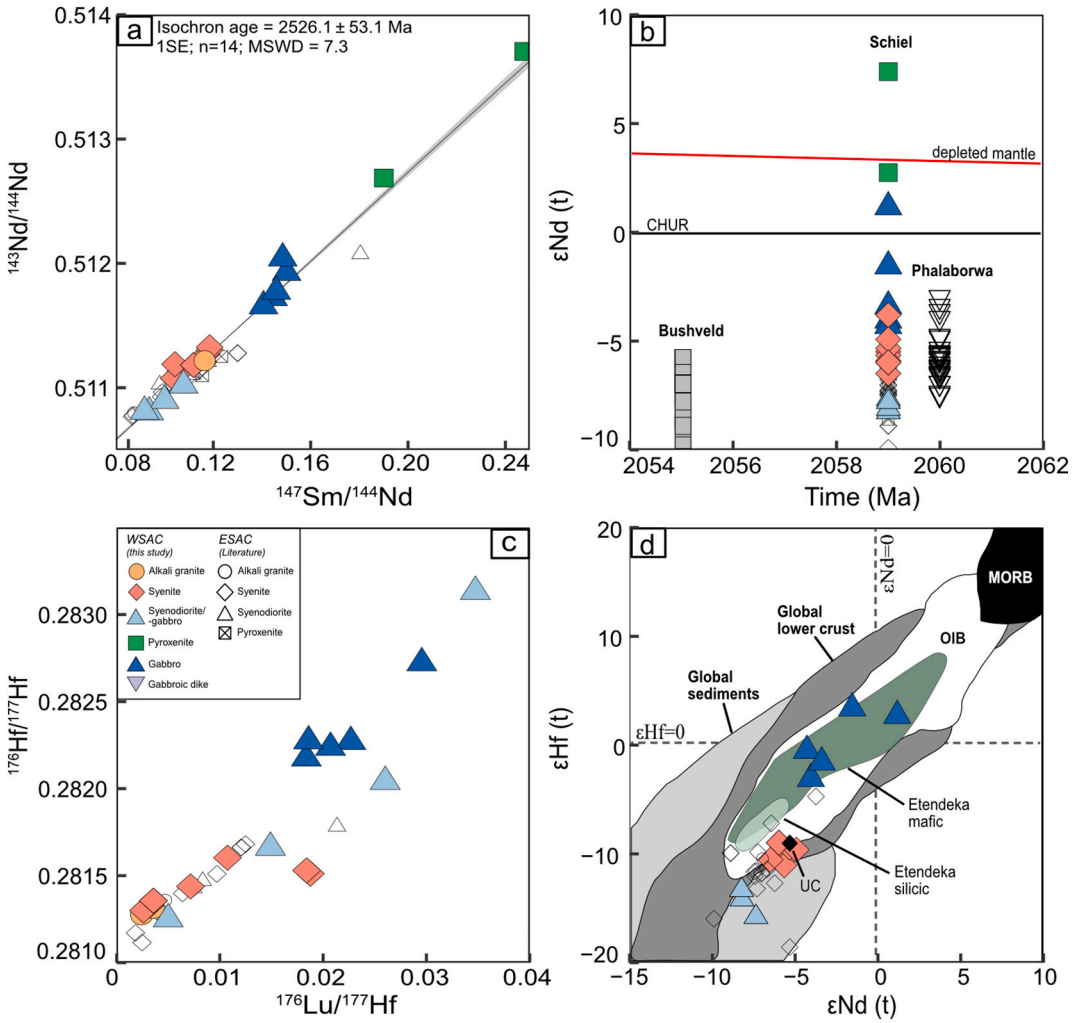


Fig. 7. (a) $^{147}Sm/^{144}Nd$ against $^{143}Nd/^{144}Nd$ in pyroxenite, gabbro, syenodiorite/−gabbro, syenite, and granite from the Schiel Complex showing an overlapping trend. (b) Epsilon neodymium (2.059 Ga) as a function of time showing the isotopic composition of the Schiel Complex. (c) $^{176}Lu/^{177}Hf$ against $^{176}Hf/^{177}Hf$ showing overlapping trends between the samples. (d) εNd against εHf of samples from the Schiel Complex and compositional fields of average ocean island basalt (OIB), mid-ocean ridge basalt (MORB), global lower crust, and global sediment (modified after Wu et al., 2011). Additional data of the eastern SAC from Graupner et al. (2018) marked by hollow symbols. Literature data of low-Ti mafic and silicic Etendeka lavas, and associated dikes (Zhou et al., 2020), and average Kaapvaal Craton upper continental crust (UC) (Hofmann, 1988; Jahn and Condie, 1995).

Ma (Fig. 7b) and both samples have high Sm/Nd and low Sm and Nd contents, which makes them very sensible for later alteration where small changes in Sm/Nd can result in significant differences in εNd. We therefore infer that post-crystallization mobilization of REE, leading to a decrease in Sm/Nd and/or increase in $^{143}Nd/^{144}Nd$, has affected the Nd isotope evolution of the highly depleted sample with εNd of +7.4 and possibly also the sample with +2.7. The gabbros, syenodiorites/−gabbros and felsic samples by contrast display higher REE concentrations and εNd values overlapping with those of Phalaborwa rocks (Fig. 7b) and were hence not significantly affected by mobilization of REE after crystallization. Nonetheless, the pyroxenites show linear correlations with the gabbros, syenites and granites in $^{143}Nd/^{144}Nd$ and $^{147}Sm/^{144}Nd$ (Fig. 7a).

Based on the spatial and temporal association of the SAC (~2.06 Ga), the Phalaborwa Complex (2.06 Ga), and the Bushveld Complex (2.05 Ga), a genetic relationship between the complexes was previously suggested (Scoates et al., 2021; Verwoerd and Du Toit, 2006; Wu et al., 2011). Such close spatial-temporal relationships were also observed between alkaline-carbonatite complexes and continental flood basalts (CFB) in other large igneous provinces (Ernst and Bell, 2010; Gibson et al., 2006). For example, the Deccan and Paranà-Etendeka flood basalts are closely associated with alkaline complexes, and based on age constraints and isotopic similarities, a genetic relation was proposed (Basu et al., 2020; Natali et al., 2018). Similarly, the western Schiel magmas show comparable isotopic and trace element compositions to primitive Bushveld lavas (Barnes et al., 2010; Zirakparvar et al., 2019). We conclude that the age data from the western SAC indicate a genetic relationship between the felsic and mafic lithologies of the entire SAC, as well as a contemporaneous formation of the magmas of the Bushveld large igneous province, including the Bushveld Complex, the SAC, and the Phalaborwa Complex.

5.2. *The formation of the SAC mafic rocks within the Bushveld large igneous province*

The origin of CFB and the associated alkaline complexes has been explained by partial melting of an upwelling hot mantle plume, by melting of the SCLM by thermal conduction from an underlying mantle plume, or by mixing of both sources (e.g., Ernst, 2014; Gibson et al., 1995; Mahoney and Coffin, 1997). For example, Ashwal (2021) suggested that the four Kaapvaal LIPs in South Africa were generated in the sub-lithospheric mantle, and that their different (isotope)geochemical

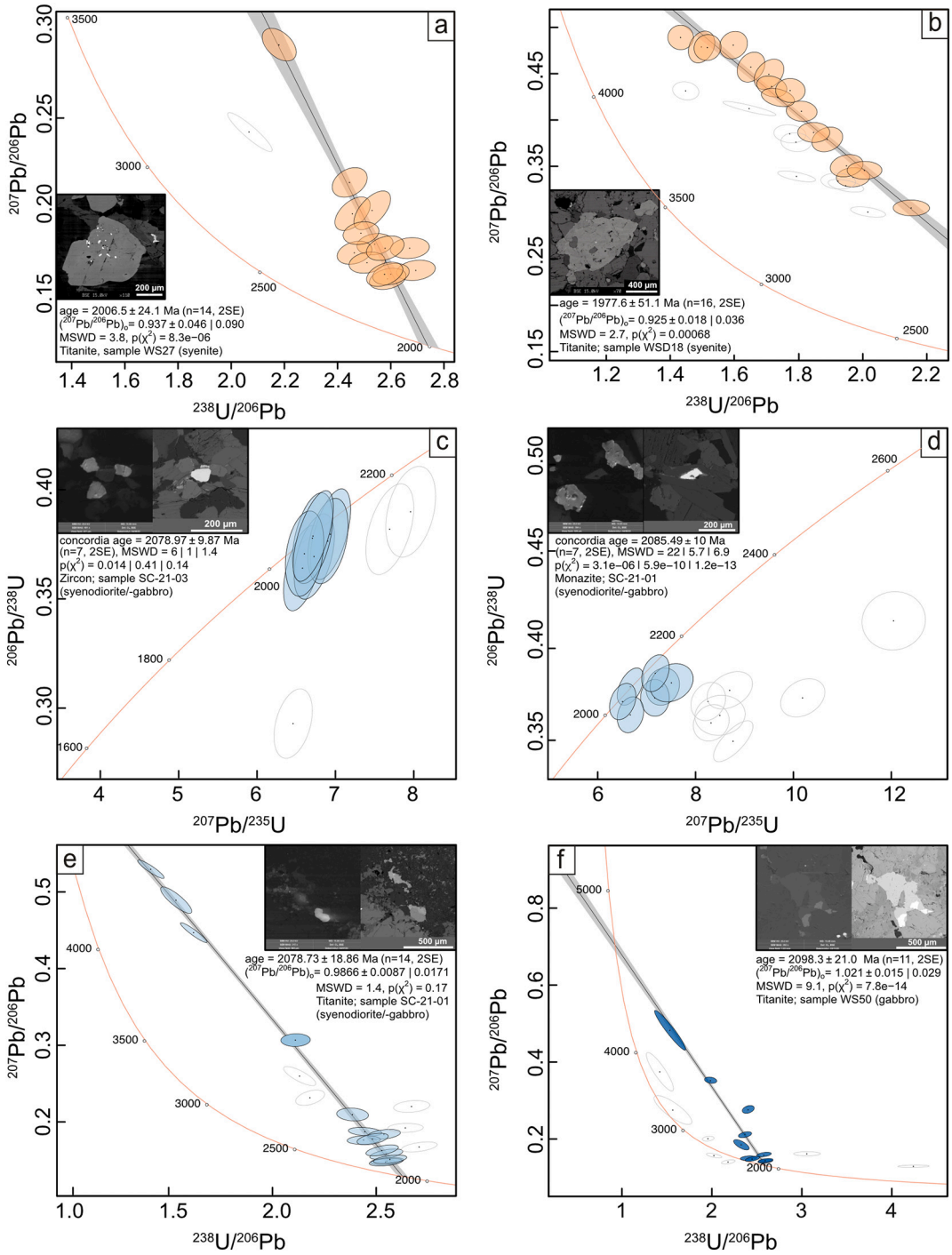


Fig. 8. Tera-Wasserburg (a, b, e, f) and Wetherill diagrams (c, d) showing isotopic compositions of titanite, monazite, and zircon in syenite (orange), syenodiorite/−gabbro (light blue), and gabbro (dark blue) from the western SAC. Microphotographs (BSE, CL) of representative grains are included for each sample. Data points variably dispersed around regression lines were excluded from the calculation (hollow circles). The uncertainty is reported as standard error 2SE. (For interpretation of the references to colour in this figure legend, the reader is referred to the web version of this article.)

signatures are due to variable assimilation of continental crustal components. However, the alkaline and carbonatite complexes associated with the LIPs in the Kaapvaal may constitute low-degree melting products that were generated locally from the SCLM during the ascent of large-volume, plume-derived melts (Ashwal, 2021; Ashwal et al., 2016). Similarly, models of younger LIPs and associated alkaline complexes, such as Paranà-Etendeka and Deccan, suggest the contemporaneous generation of CFB and alkaline melts from the mantle plume and the SCLM (Basu et al., 2020; Beccaluva et al., 2020; Natali et al., 2018).

Previous studies of the pyroxenites, syenites, and granites of the eastern Schiel Complex inferred a lithospheric mantle source enriched by subduction-related metasomatism (Barton et al., 1996; Graupner et al., 2018; Laurent and Zeh, 2015), which was also considered as the most likely source in other alkaline carbonatite complexes with similar isotopic signatures to the felsic rocks (e.g., Siegel et al., 2017). The PRIMA-normalized trace element gabbro patterns show an incompatible trace element enrichment with relatively high LREE contents and notable depletion of Nb and Ta, but an enrichment in Pb (Fig. 6c). These

enrichments are typically associated with subduction zone-related metasomatism of the mantle, but also occur in enriched mantle (EM)-type OIB (Weaver, 1991). The SAC gabbros display trace element patterns similar to those of continental flood basalts (CFB) from the Etendeka-Parana LIP of southern Africa and South America (Fig. 6e). The gabbros and pyroxenites show Nb/La ratios (Nb/La = 0.45–0.63) that are lower than those of most OIB (Nb/La > 1), but resemble those of the Tristan da Cunha/Gough EM1-type OIB and the Etendeka CFB (Fig. 9d; Natali et al., 2018 and references therein). The positive εNd and εHf of the relatively primitive western SAC gabbros and pyroxenites (Table 2) indicate an origin in a mantle that underwent time-integrated depletion, although the incompatible elements are enriched. Similar primitive magma compositions with εNd and εHf between +7 and − 5, light REE enrichment, and Nb/La <1 are known from the youngest LIP in southern Africa, namely the Etendeka flood basalts that are believed to have formed from a heterogeneous mantle plume (Zhou et al., 2020). The εNd and εHf values of the Etendeka rocks show a positive correlation comparable to that of the SAC samples (Fig. 7d), which has been interpreted to reflect increasing crustal contamination (Thompson et al., 2007). Thus, we suggest that the SAC gabbros formed from an OIB mantle comparable to that of the Cretaceous Etendeka LIP, and that the Schiel magmas (present study, Graupner et al., 2018) were possibly affected by continental crustal assimilation (Fig. 7d).

5.3. The relation between the mafic and felsic rocks of the SAC

Mafic and alkaline felsic magmas occur in many LIPs and may either be co-genetic, or the geochemical differences between CFB-related melts and alkaline melts are due to different magma sources where the ascent of CFB from the asthenosphere triggered melting in the subcontinental lithospheric mantle and the formation of alkaline complexes (Beccaluva et al., 2020; Black et al., 2021; Natali et al., 2018, Natali et al., 2013). However, in the case of the western SAC, our new age constraints suggest a nearly contemporaneous formation of the mafic and felsic rocks, implying that the mafic magmas may have been parental to the felsic melts. A magma evolution from the gabbros to syenodiorite/−gabbros, syenites, and finally alkali granites is supported by correlated trends of major element concentrations like $Fe_2O_3^T$, TiO_2 (Fig. 4c, d), MgO, CaO, and P_2O_5 (not shown) with SiO_2. Similarly, trace element concentrations of Cr and Ce show trends with SiO_2, and indicate a magma evolution by fractional crystallization from a mafic melt (Fig. 4e, f). Moreover, the syenites, granites, and gabbros show overlapping colinear relations in their Sm—Nd isotope compositions (R^2 = 9.5), which we suggest to reflect mixing between mantle- and crust-derived melts (Fig. 7a). Many

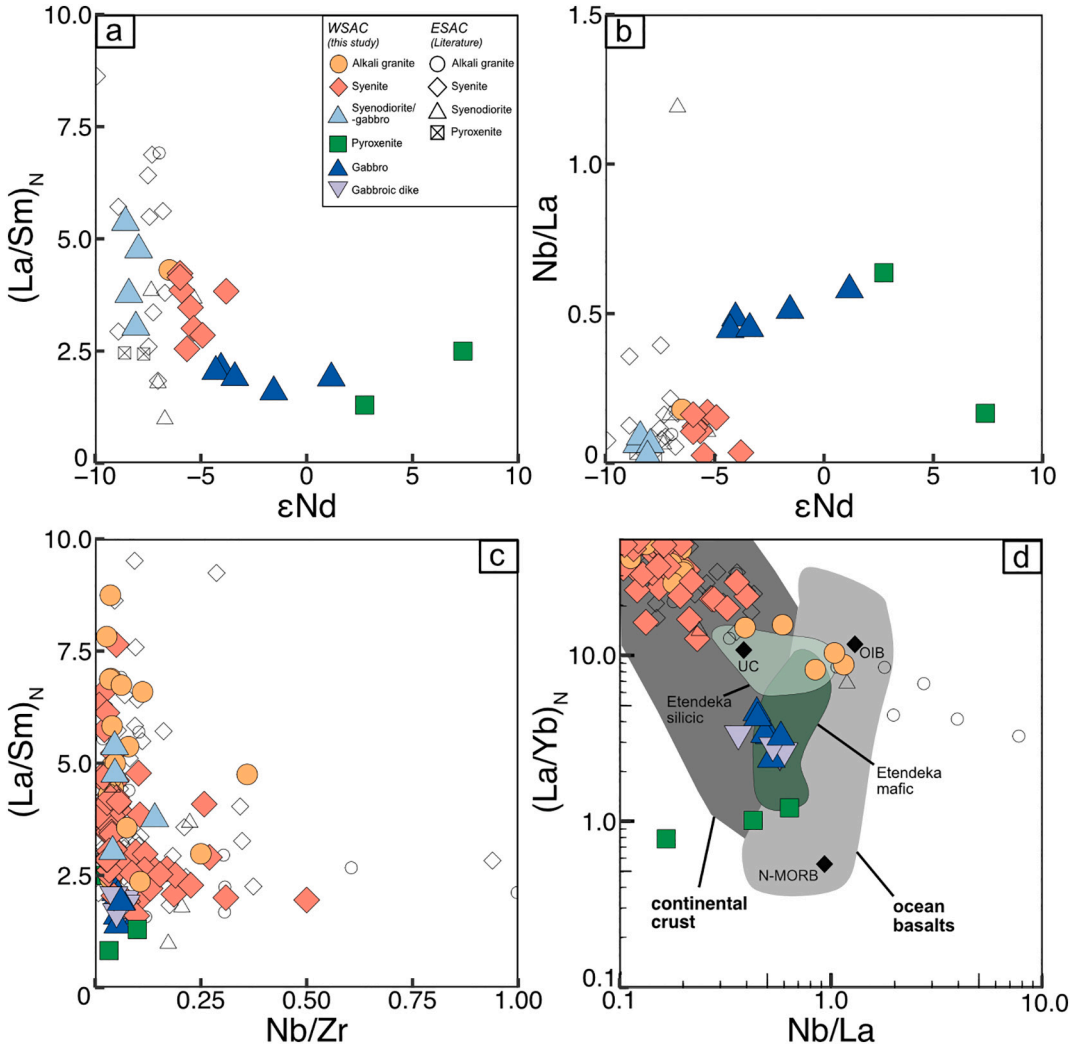


Fig. 9. Combined isotopic and trace element ratios of the different lithologies from the Schiel Complex. (a) Chondrite-normalized La/Sm against εNd showing continuous trends from the pyroxenites to the gabbros, syenites, and alkali granites. (b) Nb/La against εNd with higher Nb/La ratios for the gabbros. (c) Chondrite-normalized La/Sm against Nb/Zr showing similar Nb/Zr ratios for all lithologies but variable La/Sm ratios. (d) Normalized La/Yb against Nb/La with the compositional fields of ocean basalts and continental crust (modified after Arndt and Christensen, 1992), average OIB, upper continental crust (UC), N-MORB (Sun and McDonough, 1989), and literature data from Etendeka silicic and mafic lavas, and associated dikes for comparison (Zhou et al., 2020).

alkaline complexes show such variations from mafic to felsic compositions, i.e. from gabbros to syenites as, for example, the Messum complex in the Etendeka LIP (Trumbull, 2003) and the Barmer and Mundwara complexes in the Deccan LIP (Basu et al., 2020; Simonetti et al., 1998). Both the mafic and felsic rocks reveal negative Nb and Ta, but positive Pb anomalies, indicating a similar magma source (Fig. 6), which is also comparable to lavas from the Etendeka LIP (Zhou et al., 2020). Continuous AFC trends between mafic and felsic rocks are revealed by increasing Nb/Zr and Ba/La ratios at increasing SiO_2, where gabbros, syenites and alkali granites overlap, although the felsic rocks show a larger variance in trace element ratios (Fig. 5). Furthermore, increasing chondrite-normalized $(La/Sm)_N$ ratios with decreasing εNd show continuous and overlapping trends, indicating a liquid line of descent from a mafic component represented by the gabbros to the syenites and alkali granites (Fig. 9a). Importantly, the compositions of the gabbroic dikes fall onto the liquid line of descent (except for TiO_2), suggesting that these late intrusions may also be cogenetic to the plutons (Fig. 4, 9c). A nearly cotemporaneous emplacement of gabbroic dikes with the syenites was also observed at the Phalaborwa Complex (Wu et al., 2011).

A notable decrease of Al_2O_3 (Fig. 4b) and increase of $(Dy/Yb)_N$ (Fig. 5a) and $(La/Yb)_N$ ratios (Fig. 9d) from the gabbros to the least evolved felsic samples imply fractionation of an Al-rich, HREE-bearing mineral from the mafic melts. The increasing ratios typically reflect garnet fractionation, affecting the Al content of the magma and the fractionation of light to heavy REE (Green, 1975; Moyen, 2009). Depending on the composition of the basaltic melt and its water content, garnet may fractionate from basaltic melts at pressures of 1.3 to 1.8 GPa, i.e. at depths of >40 km. Garnet pyroxenites as well as garnet and clinopyroxene megacrysts are abundant in magmas traversing the subcontinental lithosphere (Blatter et al., 2023; Gonzaga et al., 2010). Various studies have examined garnet-peridotites in the Kaapvaal Craton before, confirming the required local stability conditions for garnet fractionation (e.g., Herzberg, 1993; Schutt and Lesher, 2010). The Kaapvaal SCLM below the SAC was estimated to range between 210 and 260 km (Ashwal, 2021). Basaltic magmas ascending through this thick and relatively cold lithospheric mantle may have started to crystallize already in the mantle, which would explain the compositional trends of the SAC mafic rocks. We therefore suggest, that deep fractionation of garnet from the parental magma before the formation of the syenites and alkali granites caused a decrease in Al_2O_3 and an increase in trace element ratios such as $(Dy/Yb)_N$.

Notably, the pyroxenites of the eastern SAC show similar accessory minerals (apatite, titanite, allanite), trace element concentrations, and isotopic compositions (εNd = −6.4 to −8.6; Graupner et al., 2018) to the syenites and granites, whereas the pyroxenites and gabbros from the western SAC have lower trace element contents, no REE-bearing minerals, and positive εNd (−4.3 to 7.4), either reflecting different sources of the two rock types, or more likely cumulate formation of the eastern SAC pyroxenites from evolved magmas. In conclusion, the age constraints, isotopic and geochemical trends rather argue for a continuous evolution of the syenites and granites from the mafic rocks. The pyroxenites most likely represent cumulates of clinopyroxene and orthopyroxene and, thus, lie on a separate trend from the other rocks.

5.4. *Compositional trends of the Schiel magmas: Evidence for fractional crystallization and crustal assimilation*

The major and incompatible element trends as well as the isotopic variations of the felsic rocks between 55 and 75 wt% SiO_2 suggest that the syenites and alkali granites probably formed largely due to fractional crystallization (FC) from a common parental magma s (Figs. 4 and 5). The decreasing MgO, CaO, and $Fe_2O_3 \pm TiO_2$ contents reflect fractionation of olivine and clinopyroxene ± Ti-magnetite. At ~64 wt% SiO_2 K-feldspar begins to fractionate causing a decrease in K_2O and Al_2O_3. A decrease in P_2O_5 and TiO_2 concentrations towards high-silica rocks marks the progressive removal of apatite and titanite, which is consistent with petrographic observations. Fractional crystallization of the major elements was modelled for the felsic rock suite using "MELTS rhyolite" (Gualda et al., 2012) with a low silica felsic sample (WSD3) as starting composition, pressures of 2, 3, 4, 5, 10 kbar, and water contents of 0.5 wt%, 1 wt%, and 2 wt%, respectively (suppl. Table A4). The modelled crystallization trends consistently match with the compositional trends defined by the felsic samples for 0.5 and 1% wt% H_2O, supporting a magma evolution by fractional crystallization at low water content (Fig. 4 a-d, FC for 1 wt% H_2O at 3 kbar shown). Low and high pressure conditions thereby produce comparable fractionation trends (supp. Table 4A). The modelled Al_2O_3 curve provides a generally poorer match, which calculated Al_2O_3 concentrations up to 3 wt% lower than the felsic rock composition and a steeper decrease at >64 wt% SiO_2. The onset and degree of feldspar fractionation, which mainly controls the Al_2O_3 curve, is pressure dependent due to either amphibole- or plagioclase- dominant crystallization (Caricchi et al., 2006) and is enhanced during low pressure magma evolution in comparison to deep fractional crystallization (Nekvasil, 2004). Especially accumulation of feldspar can shift the crystallization curve to higher aluminum contents, which can result in deviations from FC modelling.

However, fractional crystallization cannot produce the compositional trends of major elements and the large span in εNd(t) from +2.7 to −6.5 for the ultramafic to the felsic rocks. Especially the isotopic range from +1.1 to - 4.3 in εNd of the gabbros is indicative for contamination of the mafic magma (Fig. 5). The observed correlation between εHf and εNd in the SAC gabbros suggests assimilation processes similar to those affecting the Etendeka mafic rocks, whereas the felsic Etendeka and SAC syenites and alkali granites have the lowest, crust-like εHf and εNd (Fig. 7d). Additional to the variable Nd isotope compositions, anomalously enriched Pb contents (Fig. 6), and elevated Th/La (0.1–0.28) ratios of the gabbros suggest that the parental mafic melts underwent substantial crustal assimilation during ascent, since average continental crust has relatively high Th/La around 0.30 (Plank, 2005) and low Nd isotope ratios. Furthermore, the gabbros show distinctly low Ce/Pb ratios (<10) that are typical signatures of continental crust (Rudnick and Fountain, 1995). Typical crustal signatures are also visible in PRIMA-normalized trace element pattern, where the gabbros display negative Nb, Ta, Ti, and positive Pb anomalies (Fig. 6e). However, the highly potassic signature of the syenites and alkali granites suggests the involvement of a K-rich component. Assimilation-fractional crystallization (AFC) modelling using "MELTS rhyolite" (Gualda et al., 2012) was therefore conducted using one gabbro sample (WS 36) as starting composition (0.5, 1, and 2 wt% H_2O) and a metapelitic composition from the Kaapvaal craton as possible assimilant (Kreissig et al., 2000). Compositional trends were calculated as AFC for $SiO_2 < 56$ wt% and as FC for $SiO_2 > 56$ wt% using fixed pressures of 6 kbar and 3 kbar, as well as decreasing pressures from 7 kbar to 2 kbar during fractionation (suppl. Table A4). The modelled crystallization trends for K_2O, Fe_2O_3, and TiO_2 match our proposed liquid line of descent from the gabbros to the least evolved syenites at 6 kbar (Fig. 4a, c, d; dark grey and blueish lines) and 3 kbar (not shown; suppl. Table A4). The evolutionary trend from the gabbros and syenites to the evolved alkali granites can be obtained by decreasing pressures during crystallization (dark grey and blueish dotted lines, Fig. 4a, c, d). Similar to the FC modelling for the syenites and alkali granites, the modelled AFC curve of Al_2O_3 provides a poor match (Fig. 4b), possibly related to feldspar accumulation. Due to the heterogeneous composition of the continental crust beneath the Kaapvaal craton, and possible mixing of different components (e.g., metapelite), the identification of the end-member assimilant proves to be difficult. Nevertheless, the thermodynamic modelling supports an evolution of the syenites and alkali granites from the gabbros by AFC. Noteworthy, the thermodynamic modelling further indicated the fractionation of garnet at high pressures, supporting the previously proposed deep fractionation of garnet prior to the formation of the syenites (suppl. Table A4).

The similar isotopic composition of the syenites and granites at

variable MgO and SiO_2 content indicates the absence of major assimilation during formation of the felsic rocks. However, large ranges in trace element ratios (e.g., Nb/Zr, Ba/La) irrespective of their MgO and SiO_2 content suggest heterogeneous, minor crustal contamination of the syenites and alkali granites (Fig. 5d). Especially Nb concentrations are affected by assimilation due to elevated Nb contents in the crust and the syenites exhibit La/Yb and Nb/La ratios that align with the compositional range of the continental crust (Fig. 9d). Moreover, the Schiel magmas, particularly the gabbros, gabbroic dikes, and alkali granites, display variations resembling those observed in lavas from the Etendeka LIP (Fig. 9d). In addition, the respective T(DM) model ages (3.1.–2.2 Ga), and the apparent Sm—Nd isochron ages (2526 Ma, 2211 Ma) are significantly older than the crystallization age, thereby revealing strong evidence for an ancient crustal contribution. We propose contamination of the hot mafic magmas in the continental crust, which appears to be typical for LIP magmas during the ascent and is also observed in the Etendeka lavas (Beccaluva et al., 2020; Zhou et al., 2020). In contrast, the SAC syenites and granites were only moderately affected by crustal assimilation and their chemical variation formed primarily by fractional crystallization.

6. Conclusions

This study reports the first geochemical and isotopic analyses of the western SAC providing new insights into the formation of the complex. New $^{238}U/^{206}Pb$ intercept ages of titanite and concordant zircon and monazite ages suggest a co-genetic evolution of the mafic and felsic rocks. Continuous and overlapping isotopic compositions, major and trace element trends, and incompatible element ratios support the evolution of the syenites and granites from a mafic melt that is represented by the gabbros. Interestingly, the observed compositional trends of the SAC rocks resemble those of lavas and plutonic rocks of the Cretaceous Etendeka LIP. For the first time, radiogenic Nd isotope signatures (positive εNd, εHf) were found in primitive SAC magmas suggesting an OIB mantle as magma source and, thus, formation of the magmas in a mantle plume. The mafic magmas assimilated continental crustal material during ascent, which is evident from incompatible element signatures and varying isotopic compositions. Fractional crystallization dominated the magmatic evolution from the mafic to the intermediate rocks with a possible role of garnet fractionation deep in the lithosphere prior to emplacement. The more evolved samples were only moderately and heterogeneously affected by crustal contamination.

Statements and declarations

Funding of this project was provided by the Bundesanstalt für Geowissenschaften und Rohstoffe [grant 212-10100724], which is gratefully acknowledged. The authors declare no relevant financial or non-financial interests to disclose.

Declaration of Competing Interest

The authors declare that they have no known competing financial interests or personal relationships that could have appeared to influence the work reported in this paper.

Acknowledgements

We thank M. Hertel for help with the XRF analyses and M. Regelous for the support with the isotopic measurements. We would further like to thank the two anonymous reviewers, whose comments greatly improved this manuscript. Furthermore, we want to thank Günter Brandl for support during the field work, and Christoph Beier and Jock Harmer for discussions concerning the thermodynamic modelling.

Appendix A. Supplementary data

Supplementary data to this article can be found online at https://doi.org/10.1016/j.lithos.2023.107464.

References

Arndt, N.T., Christensen, U., 1992. The role of lithospheric mantle in continental flood volcanism: thermal and geochemical constraints. J. Geophys. Res. 97, 10967. https://doi.org/10.1029/92JB00564.

Ashwal, L.D., 2021. Sub-lithospheric mantle sources for overlapping southern African Large Igneous Provinces. S. Afr. J. Geol. 124, 421–442. https://doi.org/10.25131/sajg.124.0023.

Ashwal, L.D., Patzelt, M., Schmitz, M.D., Burke, K., 2016. Isotopic evidence for a lithospheric origin of alkaline rocks and carbonatites: an example from southern Africa. Can. J. Earth Sci. 53, 1216–1226. https://doi.org/10.1139/cjes-2015-0145.

Barnes, S.-J., Maier, W.D., Curl, E.A., 2010. Composition of the Marginal Rocks and Sills of the Rustenburg Layered Suite, Bushveld Complex, South Africa: Implications for the Formation of the Platinum-Group Element Deposits. Econ. Geol. 105, 1491–1511. https://doi.org/10.2113/econgeo.105.8.1491.

Barton, J.M., Barton, E.S., Smith, C.B., 1996. Petrography, age and origin of the Schiel alkaline complex, northern Transvaal, South Africa. J. Afr. Earth Sci. 22, 133–145. https://doi.org/10.1016/0899-5362(96)00005-X.

Barton, J.M., Klemd, R., Zeh, A., 2006. The Limpopo Belt: A result of Archean to Proterozoic, Turkic-type orogenesis? In: Reimold, W.U., Gibson, R.L. (Eds.), Processes on the Early Earth. Geological Society of America, pp. 315–332. https://doi.org/10.1130/2006.2405(16).

Basu, A.R., Renne, P.R., DasGupta, D.K., Teichmann, F., Poreda, R.J., 1993. Early and Late Alkali Igneous Pulses and a High- ^{3} He Plume Origin for the Deccan Flood Basalts. Science 261, 902–906. https://doi.org/10.1126/science.261.5123.902.

Basu, A.R., Chakrabarty, P., Szymanowski, D., Ibañez-Mejia, M., Schoene, B., Ghosh, N., Georg, R.B., 2020. Widespread silicic and alkaline magmatism synchronous with the Deccan Traps flood basalts, India. Earth Planet. Sci. Lett. 552, 116616 https://doi.org/10.1016/j.epsl.2020.116616.

Beccaluva, L., Bianchini, G., Natali, C., Siena, F., 2020. Plume-related Paranà-Etendeka igneous province: an evolution from plateau to continental rifting and breakup. Lithos 362–363, 105484. https://doi.org/10.1016/j.lithos.2020.105484.

Black, B.A., Karlstrom, L., Mather, T.A., 2021. The life cycle of large igneous provinces. Nat. Rev. Earth Environ. 2, 840–857. https://doi.org/10.1038/s43017-021-00221-4.

Blatter, D.L., Sisson, T.W., Hankins, W.B., 2023. Garnet stability in arc basalt, andesite, and dacite—an experimental study. Contrib. Mineral. Petrol. 178, 33. https://doi.org/10.1007/s00410-023-02008-w.

Blichert-Toft, J., Puchtel, I.S., 2010. Depleted mantle sources through time: evidence from Lu–Hf and Sm–Nd isotope systematics of Archean komatiites. Earth Planet. Sci. Lett. 297, 598–606. https://doi.org/10.1016/j.epsl.2010.07.012.

Bolhar, R., Wilson, A., Tusch, J., Pettke, T., Hasenstab-Dübeler, E., Fischer-Gödde, M., Anhaeusser, C., 2023. Reworking of aged mafic crust in a Palaeoarchaean layered complex inferred from coupled Sm-Nd and Lu-Hf isotope systematics, Stolzburg Complex, Barberton Greenstone Belt, South Africa. Chem. Geol. 626, 121427 https://doi.org/10.1016/j.chemgeo.2023.121427.

Bouvier, A., Vervoort, J.D., Patchett, P.J., 2008. The Lu–Hf and Sm–Nd isotopic composition of CHUR: Constraints from unequilibrated chondrites and implications for the bulk composition of terrestrial planets. Earth Planet. Sci. Lett. 273, 48–57. https://doi.org/10.1016/j.epsl.2008.06.010.

Caricchi, L., Ulmer, P., Peccerillo, A., 2006. A high-pressure experimental study on the evolution of the silicic magmatism of the Main Ethiopian Rift. Lithos 91, 46–58. https://doi.org/10.1016/j.lithos.2006.03.008.

Chauvel, C., Dupré, B., Jenner, G.A., 1985. The Sm-Nd age of Kambalda volcanics is 500 Ma too old! Earth Planet. Sci. Lett. 74, 315–324. https://doi.org/10.1016/S0012-821X(85)80003-0.

Chauvel, C., Bureau, S., Poggi, C., 2011. Comprehensive Chemical and Isotopic analyses of Basalt and Sediment Reference Materials. Geostand. Geoanal. Res. 35, 125–143. https://doi.org/10.1111/j.1751-908X.2010.00086.x.

Cherniak, D.J., 1993. Lead diffusion in titanite and preliminary results on the effects of radiation damage on Pb transport. Chem. Geol. 110, 177–194. https://doi.org/10.1016/0009-2541(93)90253-F.

Cherniak, D.J., Watson, E.B., Grove, M., Harrison, T.M., 2004. Pb diffusion in monazite: a combined RBS/SIMS study. Geochim. Cosmochim. Acta 68, 829–840. https://doi.org/10.1016/j.gca.2003.07.012.

Corfu, F., 2003. Atlas of Zircon Textures. Rev. Mineral. Geochem. 53, 469–500. https://doi.org/10.2113/0530469.

Cox, K.G., Bell, J.D., Pankhurst, R.J., 1979. The Interpretation of Igneous Rocks, 1 (publ. ed).

Decrée, S., Cawthorn, G., Deloule, E., Mercadier, J., Frimmel, H., Baele, J.-M., 2020. Unravelling the processes controlling apatite formation in the Phalaborwa complex (South Africa) based on combined cathodoluminescence, LA-ICPMS and in-situ O and Sr isotope analyses. Contrib. Mineral. Petrol. 175 https://doi.org/10.1007/s00410-020-1671-6.

Du Toit, M.C., 1979. Die geologie en struktuur van die gebiedeLevubu en Bandelierkorp in Noord-Transvaal.

Ernst, R.E., 2014. Large igneous provinces. Cambridge University Press, New York.

Ernst, R.E., Bell, K., 2010. Large igneous provinces (LIPs) and carbonatites. Mineral. Petrol. 98, 55–76. https://doi.org/10.1007/s00710-009-0074-1.

Gibson, S.A., Thompson, R.N., Dickin, A.P., Leonardos, O.H., 1995. High-Ti and low-Ti mafic potassic magmas: Key to plume-lithosphere interactions and continental flood-basalt genesis. Earth Planet. Sci. Lett. 136, 149–165. https://doi.org/10.1016/0012-821X(95)00179-G.

Gibson, S.A., Thompson, R.N., Day, J.A., 2006. Timescales and mechanisms of plume–lithosphere interactions: 40Ar/39Ar geochronology and geochemistry of alkaline igneous rocks from the Paraná–Etendeka large igneous province. Earth Planet. Sci. Lett. 251, 1–17. https://doi.org/10.1016/j.epsl.2006.08.004.

Gonzaga, R.G., Lowry, D., Jacob, D.E., LeRoex, A., Schulze, D., Menzies, M.A., 2010. Eclogites and garnet pyroxenites: Similarities and differences. J. Volcanol. Geotherm. Res. 190, 235–247. https://doi.org/10.1016/j.jvolgeores.2009.08.022.

Graupner, T., Klemd, R., Henjes-Kunst, F., Goldmann, S., Behnsen, H., Gerdes, A., Dohrmann, R., Barton, J.M., Opperman, R., 2018. Formation conditions and REY enrichment of the 2060 Ma phosphorus mineralization at Schiel (South Africa): geochemical and geochronological constraints. Mineral. Deposita 53, 1117–1142. https://doi.org/10.1007/s00126-018-0791-7.

Green, D.H., 1975. Genesis of Archaean periotitic magmas and constraints on Archaean geothermal gradients and tectonics. Geology 15–18.

Gualda, G.A.R., Ghiorso, M.S., Lemons, R.V., Carley, T.L., 2012. Rhyolite-MELTS: a Modified Calibration of MELTS Optimized for Silica-rich, Fluid-bearing Magmatic Systems. J. Petrol. 53, 875–890. https://doi.org/10.1093/petrology/egr080.

Hatton, C.J., 1995. Mantle plume origin for the Bushveld and Ventersdorp magmatic provinces. J. Afr. Earth Sci. 21, 571–577. https://doi.org/10.1016/0899-5362(95)00106-9.

Herzberg, C.T., 1993. Lithosphere peridotites of the Kaapvaal craton. Earth Planet. Sci. Lett. 120, 13–29. https://doi.org/10.1016/0012-821X(93)90020-A.

Hofmann, A.W., 1988. Chemical differentiation of the Earth: the relationship between mantle, continental crust, and oceanic crust. Earth Planet. Sci. Lett. 90, 297–314. https://doi.org/10.1016/0012-821X(88)90132-X.

Jahn, B.-M., Condie, K.C., 1995. Evolution of the Kaapvaal Craton as viewed from geochemical and Sm-Nd isotopic analyses of intracratonic pelites. Geochim. Cosmochim. Acta 59, 2239–2258. https://doi.org/10.1016/0016-7037(95)00103-7.

Kamo, S.L., Reimold, W.U., Krogh, T.E., Colliston, W.P., 1996. A 2.023 Ga age for the Vredefort impact event and a first report of shock metamorphosed zircons in pseudotachylitic breccias and Granophyre. Earth Planet. Sci. Lett. 144, 369–387. https://doi.org/10.1016/S0012-821X(96)00180-X.

Kreissig, K., Nägler, T.F., Kramers, J.D., van Reenen, D.D., Smit, C.A., 2000. An isotopic and geochemical study of the northern Kaapvaal Craton and the Southern Marginal Zone of the Limpopo Belt: are they juxtaposed terranes? Lithos 50, 1–25. https://doi.org/10.1016/S0024-4937(99)00037-7.

Laurent, O., Zeh, A., 2015. A linear Hf isotope-age array despite different granitoid sources and complex Archean geodynamics: example from the Pietersburg block (South Africa). Earth Planet. Sci. Lett. 430, 326–338. https://doi.org/10.1016/j.epsl.2015.08.028.

Le Bras, L.Y., Milani, L., Bolhar, R., O'Sullivan, G., 2022. Applying U-Pb chronometry and trace element geochemistry of apatite to carbonatite-phoscorite complexes – as exemplified by the 2.06 Ga Phalaborwa complex, South Africa. S. Afr. J. Geol. 125, 179–190. https://doi.org/10.25131/sajg.125.0015.

Lugmair, G.W., Marti, K., 1978. Lunar initial 143Nd/144Nd: Differential evolution of the lunar crust and mantle. Earth Planet. Sci. Lett. 39, 349–357. https://doi.org/10.1016/0012-821X(78)90021-3.

Mahoney, J.J., Coffin, M.F. (Eds.), 1997. Large Igneous Provinces: Continental, Oceanic, and Planetary Flood Volcanism: Mahoney/Large Igneous Provinces: Continental, Oceanic, and Planetary Flood Volcanism, Geophysical Monograph Series. American Geophysical Union, Washington, D. C. https://doi.org/10.1029/GM100.

Mariano, A.N., 1989. Nature of economic mineralization in carbonatites and related rocks. Carbonat. Genesis Evol. 149–175.

Mason, R., 1973. A Discussion on the evolution of the Precambrian crust - the Limpopo mobile belt — Southern Africa. Phil. Trans. R. Soc. Lond. A 273, 463–485. https://doi.org/10.1098/rsta.1973.0012.

McDonough, W.F., 1990. Constraints on the composition of the continental lithospheric mantle. Earth Planet. Sci. Lett. 101, 1–18. https://doi.org/10.1016/0012-821X(90)90119-I.

McDonough, W.F., Sun, S., 1995. The composition of the Earth. Chem. Geol. 120, 223–254.

Miyashiro, A., 1978. Nature of alkalic volcanic rock series. Contrib. Mineral. Petrol. 66, 91–104. https://doi.org/10.1007/BF00376089.

Moyen, J.-F., 2009. High Sr/Y and La/Yb ratios: The meaning of the "adakitic signature". Lithos 112, 556–574. https://doi.org/10.1016/j.lithos.2009.04.001.

Mungall, J.E., Kamo, S.L., McQuade, S., 2016. U–Pb geochronology documents out-of-sequence emplacement of ultramafic layers in the Bushveld Igneous Complex of South Africa. Nat. Commun. 7, 13385. https://doi.org/10.1038/ncomms13385.

Myeong, B., Regelous, M., Haase, K.M., Münker, C., 2023. Effects of variable slab components and tectonics on magma composition in the intra-oceanic Kermadec Arc-Backarc system. Chem. Geol. 616, 121246 https://doi.org/10.1016/j.chemgeo.2022.121246.

Natali, C., Beccaluva, L., Bianchini, G., Ellam, R.M., Siena, F., Stuart, F.M., 2013. Carbonated alkali-silicate metasomatism in the North Africa lithosphere: evidence from Middle Atlas spinel-lherzolites, Morocco. J. S. Am. Earth Sci. 41, 113–121. https://doi.org/10.1016/j.jsames.2012.06.014.

Natali, C., Beccaluva, L., Bianchini, G., Siena, F., 2018. Coexistence of alkaline-carbonatite complexes and high-MgO CFB in the Paranà-Etendeka province: Insights on plume-lithosphere interactions in the Gondwana realm. Lithos 296–299, 54–66. https://doi.org/10.1016/j.lithos.2017.11.001.

Nekvasil, H., 2004. The origin and evolution of silica-saturated alkalic suites: an experimental study. J. Petrol. 45, 693–721. https://doi.org/10.1093/petrology/egg103.

Paton, C., Hellstrom, J., Paul, B., Woodhead, J., Hergt, J., 2011. Iolite: Freeware for the visualisation and processing of mass spectrometric data. J. Anal. At. Spectrom. 26, 2508. https://doi.org/10.1039/c1ja10172b.

Petrus, J.A., Kamber, B.S., 2012. Vizual age: a novel approach to laser ablation ICP-MS U-Pb geochronology data reduction. Geostand. Geoanal. Res. 36, 247–270. https://doi.org/10.1111/j.1751-908X.2012.00158.x.

Plank, T., 2005. Constraints from Thorium/Lanthanum on Sediment Recycling at Subduction zones and the Evolution of the Continents. J. Petrol. 46, 921–944. https://doi.org/10.1093/petrology/egi005.

Roering, C., van Reenen, D.D., Smit, C.A., Barton, J.M., Beer, J.H., Wit, M.J., Stettler, E.H., van Schalkwyk, J.F., Stevens, G., Pretorius, S., 1992. Tectonic model for the evolution of the Limpopo Belt. Precambrian Res. 55, 539–552. https://doi.org/10.1016/0301-9268(92)90044-O.

Rudnick, R.L., Fountain, D.M., 1995. Nature and composition of the continental crust: a lower crustal perspective. Rev. Geophys. 33, 267. https://doi.org/10.1029/95RG01302.

Rudnick, R.L., Gao, S., 2014. Composition of the Continental crust. In: Treatise on Geochemistry. Elsevier, pp. 1–51. https://doi.org/10.1016/B978-0-08-095975-7.00301-6.

Schutt, D.L., Lesher, C.E., 2010. Compositional trends among Kaapvaal Craton garnet peridotite xenoliths and their effects on seismic velocity and density. Earth Planet. Sci. Lett. 300, 367–373. https://doi.org/10.1016/j.epsl.2010.10.018.

Scoates, J.S., Wall, C.J., Friedman, R.M., Weis, D., Mathez, E.A., VanTongeren, J.A., 2021. Dating the Bushveld Complex: timing of Crystallization, Duration of Magmatism, and Cooling of the World's Largest Layered Intrusion and Related Rocks. J. Petrol. 62, egaa107. https://doi.org/10.1093/petrology/egaa107.

Siegel, K., Williams-Jones, A.E., Stevenson, R., 2017. A Nd- and O-isotope study of the REE-rich peralkaline Strange Lake granite: implications for Mesoproterozoic A-type magmatism in the Core Zone (NE-Canada). Contrib. Mineral. Petrol. 172 https://doi.org/10.1007/s00410-017-1373-x.

Simonetti, A., Bell, K., Viladkar, S.G., 1995. Isotopic data from the Amba Dongar Carbonatite complex, west-Central India: evidence for an enriched mantle source. Chem. Geol. 122, 185–198. https://doi.org/10.1016/0009-2541(95)00004-6.

Simonetti, A., Goldstein, S.L., Schmidberger, S.S., Viladkar, S.G., 1998. Geochemical and Nd, Pb, and Sr isotope data from deccan alkaline complexes—inferences for mantle sources and plume-lithosphere interaction. J. Petrol. 39, 1847–1864. https://doi.org/10.1093/petroj/39.11-12.1847.

Söderlund, U., Patchett, P.J., Vervoort, J.D., Isachsen, C.E., 2004. The 176Lu decay constant determined by Lu–Hf and U–Pb isotope systematics of Precambrian mafic intrusions. Earth Planet. Sci. Lett. 219, 311–324. https://doi.org/10.1016/S0012-821X(04)00012-3.

Stettler, E.H., Coetzee, H., Rogers, H.J.J., Lubala, R.T., 1993. The Schiel Alkaline complex: geological setting and geophysical investigation. S. Afr. J. Geol. 96, 96–107.

Sun, S., McDonough, W.F., 1989. Chemical and isotopic systematics of oceanic basalts: implications for mantle composition and processes. Geol. Soc. Lond. Spec. Publ. 42, 313–345. https://doi.org/10.1144/GSL.SP.1989.042.01.19.

Taylor, R.J.M., Kirkland, C.L., Clark, C., 2016. Accessories after the facts: Constraining the timing, duration and conditions of high-temperature metamorphic processes. Lithos 264, 239–257. https://doi.org/10.1016/j.lithos.2016.09.004.

Thompson, R.N., Riches, A.J.V., Antoshechkina, P.M., Pearson, D.G., Nowell, G.M., Ottley, C.J., Dickin, A.P., Hards, V.L., Nguno, A.-K., Niku-Paavola, V., 2007. Origin of CFB Magmatism: Multi-tiered Intracrustal Picrite-Rhyolite Magmatic Plumbing at Spitzkoppe, Western Namibia, during early cretaceous Etendeka Magmatism. J. Petrol. 48, 1119–1154. https://doi.org/10.1093/petrology/egm012.

Trumbull, R.B., 2003. The Petrology of Basanite-Tephrite Intrusions in the Erongo complex and Implications for a Plume Origin of cretaceous Alkaline Complexes in Namibia. J. Petrol. 44, 93–112. https://doi.org/10.1093/petrology/44.1.93.

van Reenen, D.D., Kramers, J.D., McCourt, S., Perchuk, L.L., 2011a. Origin and evolution of Precambrian High-Grade Gneiss Terranes, with Special Emphasis on the Limpopo Complex of Southern Africa. Geol. Soc. Am. https://doi.org/10.1130/MEM207.

van Reenen, D.D., Smit, C.A., Perchuk, L.L., Roering, C., Boshoff, R., 2011b. Thrust exhumation of the Neoarchean ultrahigh-temperature Southern Marginal Zone, Limpopo Complex: Convergence of decompression-cooling paths in the hanging wall and prograde P-T paths in the footwall, in: Origin and Evolution of Precambrian High-Grade Gneiss Terranes, with special Emphasis on the Limpopo Complex of Southern Africa. Geol. Soc. Am. https://doi.org/10.1130/2011.1207(11.

Vermeesch, P., 2018. IsoplotR: a free and open toolbox for geochronology. Geosci. Front. 9, 1479–1493. https://doi.org/10.1016/j.gsf.2018.04.001.

Verwoerd, W., Du Toit, M., 2006. The Phalaborwa and Schiel complexes. In: Johnsin, M. R. (Ed.), The Geology of South Africa. Geological Society of South Africa, Pretoria, pp. 291–300.

Verwoerd, W.J., Viljoen, E.A., Chevallier, L., 1995. Rare metal mineralization at the Salpeterkop carbonatite complex, Western Cape Province, South Africa. J. Afr. Earth Sci. 21, 171–186. https://doi.org/10.1016/0899-5362(95)00085-8.

Walraven, F., Frick, C., Lubala, R.T., 1992. Pb-isotope geochronology of the Schiel complex, Northern Transvaal, South Africa. J. Afr. Earth Sci. 15, 103–110. https://doi.org/10.1016/0899-5362(92)90011-Z.

Weaver, B.L., 1991. The origin of ocean island basalt end-member compositions: trace element and isotopic constraints. Earth Planet. Sci. Lett. 104, 381–397. https://doi.org/10.1016/0012-821X(91)90217-6.

Wilson, M., 1989. Igneous Petrogenesis. Springer, Netherlands, Dordrecht. https://doi.org/10.1007/978-1-4020-6788-4.

Wu, F.-Y., Yang, Y.-H., Li, Q.-L., Mitchell, R.H., Dawson, J.B., Brandl, G., Yuhara, M., 2011. In situ determination of U–Pb ages and Sr–Nd–Hf isotopic constraints on the petrogenesis of the Phalaborwa carbonatite Complex, South Africa. Lithos 127, 309–322. https://doi.org/10.1016/j.lithos.2011.09.005.

Zhou, H., Hoernle, K., Geldmacher, J., Hauff, F., Homrighausen, S., Garbe-Schönberg, D., Jung, S., 2020. Geochemistry of Etendeka magmatism: Spatial heterogeneity in the Tristan-Gough plume head. Earth Planet. Sci. Lett. 535, 116123 https://doi.org/10.1016/j.epsl.2020.116123.

Zirakparvar, N.A., Mathez, E.A., Rajesh, H.M., Choe, S., 2019. Lu-Hf isotopic evidence of a deep mantle plume source for the ~2.06 Ga Bushveld large Igneous Province. Lithos 348–349, 105168. https://doi.org/10.1016/j.lithos.2019.105168.